

2014

# Experiments on Surfactants and Thin Fluid Films

Peter Megson  
*Harvey Mudd College*

---

## Recommended Citation

Megson, Peter, "Experiments on Surfactants and Thin Fluid Films" (2014). *HMC Senior Theses*. 64.  
[https://scholarship.claremont.edu/hmc\\_theses/64](https://scholarship.claremont.edu/hmc_theses/64)

This Open Access Senior Thesis is brought to you for free and open access by the HMC Student Scholarship at Scholarship @ Claremont. It has been accepted for inclusion in HMC Senior Theses by an authorized administrator of Scholarship @ Claremont. For more information, please contact [scholarship@cuc.claremont.edu](mailto:scholarship@cuc.claremont.edu).

# Experiments on Surfactants and Thin Fluid Films

**Peter Megson**

Rachel Levy, Advisor

Jon Jacobsen, Reader



**Department of Mathematics**

May, 2014

Copyright © 2014 Peter Megson.

The author grants Harvey Mudd College and the Claremont Colleges Library the nonexclusive right to make this work available for noncommercial, educational purposes, provided that this copyright statement appears on the reproduced materials and notice is given that the copying is by permission of the author. To disseminate otherwise or to republish requires written permission from the author.



The author is also making this work available under a Creative Commons Attribution–NonCommercial–ShareAlike license.

See <http://creativecommons.org/licenses/by-nc-sa/3.0/> for a summary of the rights given, withheld, and reserved by this license and <http://creativecommons.org/licenses/by-nc-sa/3.0/legalcode> for the full legal details.

# Abstract

We investigate the spatiotemporal dynamics of a surfactant monolayer on a thin fluid film spreading inward into a region devoid of surfactant, a system motivated by the alveolus of the human lung. We perform experiments that simultaneously measure the fluid height profile and the fluorescence intensity due to our fluorescent surfactant, NBD-PC. We perform experiments on both a Newtonian layer of glycerol and a shear-thinning fluid layer consisting of xanthan gum mixed with glycerol. We can very successfully extract height profiles on the xanthan gum fluid, although the simultaneous measurement of fluorescent intensity profiles proved problematic, as the laser tended to stymie the fluorescent intensity measurement. We attempt and find some success with simply measuring surfactant fluorescent intensity by itself and reconstructing behavior between the two separate measurements. We were ultimately able to make a comparative measurement of the velocity of the leading edge of surfactant on xanthan gum and glycerol.



# Acknowledgments

A lab capable of performing studies of surfactant dynamics such as those described in this thesis did not exist at Harvey Mudd College one year ago. At that time, the lab space we are currently using was not in use. Over the summer, the lab space was established by the industriousness of my fellow students: Sagar Batchu, Caitlyn Bonilla, Jeanette Liu, Shreyas Kumar, Joana Perdomo, who were helped along by the guidance of Professor Levy and the invaluable Stephen Strickland and his own advisor Professor Karen Daniels. The technical intervention of Paul Stovall and Walter Cook was inestimable in devising and building our apparatus. The members of the Harvey Mudd Chemistry Department, especially Kim Young, Penny Manisco, Daniel Guerra, and Professor Van Hecke, have been exceedingly accommodating with both their time and lab space. Professor Babak Sanii has been both helpful to our lab group and knowledgeable in equal, tremendous measure, and Professor Jon Jacobsen has been very generous with his time in reading this thesis. I'd also like to thank those people who will be taking the reigns after my departure: the members of our lab already mentioned, with the addition of Dina Sinclair and Nathaniel Leslie. Finally, I want to acknowledge the NSF (NSF-FRG-0968154) and Research Corporation (Award 19788) for supporting this project.



# Contents

<b>Abstract</b>	<b>iii</b>
<b>Acknowledgments</b>	<b>v</b>
<b>1 Introduction</b>	<b>1</b>
<b>2 Background</b>	<b>3</b>
2.1 Our System . . . . .	4
2.2 The Model . . . . .	9
<b>3 The Experiment</b>	<b>13</b>
3.1 The Apparatus . . . . .	13
3.2 Measuring Variables of Interest . . . . .	18
3.3 Laboratory Methods . . . . .	20
3.4 Image Processing . . . . .	23
<b>4 Results</b>	<b>35</b>
4.1 A New Fluid Layer . . . . .	35
4.2 Hole Closure on Glycerol and Xanthan Gum . . . . .	37
<b>5 Conclusion</b>	<b>49</b>
5.1 Discussion of Results . . . . .	49
5.2 Future Work . . . . .	50
<b>Bibliography</b>	<b>53</b>



# List of Figures

2.1	Schematic diagram showing the effect of cohesive forces on molecules in the bulk of a fluid layer and those one the surface. The molecules on the surface feel a net cohesive force pointing inwards. This gives rise to surface tension. . . . .	5
2.2	Two possible surfactant behaviors on a fluid. The surfactant molecules at the interface all align with their hydrophilic heads in the water, forming a monolayer. The surfactant molecules can also form spherical micelles, with the hydrophilic heads facing outward and the hydrophobic tails facing inward, which allows the micelle to enter the fluid bulk. . . . .	6
2.3	Molecular models of two surfactant molecules. Note the polar heads (the bunched up regions of molecules on the right side of both molecules) and non-polar tails (the long molecular chains on the left side of both) as well as the fluorophore structure on the NBD-PC molecule (this is the ring on the lower tail). Images from Avanti Polar Lipids (ava, 2013) . . .	7
3.1	The experimental apparatus in laboratory setting, with major parts labelled. The experimental system is contained by the well where the camera has visual access to it. The LEDs and laser both illuminate the well for the purposes of fluorescence imaging and laser profilometry, respectively. The ring allows us to enforce initial conditions, and the ring lifting mechanism automatically removes the ring when we wish the experiment to start. . . . .	14
3.2	Fluorescence intensity vs surfactant concentration as a fraction of the critical micelle concentration $\Gamma_c$ . Note the non-monotonic but piecewise linear shape. Figure taken from Strickland et al. (2013). . . . .	18

3.3	Schematic of laser line mechanism. Because the laser sheet is flat, the location of its intersection with the fluid is linearly related to the height of the fluid layer. . . . .	20
3.4	A schematic diagram showing the geometry involved in aligning the laser. By that the laser sheet hits the ring at the same point on both the front and back edge, we can geometrically ensure that the laser hits the substrate along the diameter of the ring. . . . .	21
3.5	The image of our ring before and after convolution. Note the locations of the bright spots in 3.5a, which correspond to the centers of the bright circles in 3.5b. The center of our ring, as found by the Hough Transform, is the bright point at the center of the image where the circles intersect. . . . .	27
3.6	An schematic showing the dependence of sample size on radius using an azimuthal averaging scheme. The larger circle passes through more bins than the smaller, thus it will be averaged over a larger sample size. . . . .	29
3.7	Calculated laser line in greensuperimposed on an image of the laser line at three moments in time. . . . .	31
3.8	Four spatially averaged height profile datasets superimposed on the noisy data, with varying size of span. As the sample size increases, the spatially averaged data (in red) becomes less noisy, as visible especially in the flat wings of the dataset, but the significant differences (i.e. the peaks) also begin to get smoothed out at some point. . . . .	32
4.1	Surfactant droplets visible on different fluid layers . . . . .	36
4.2	Time series of images of a inward spreading data run on a glycerol fluid layer. Our initial concentration is $\Gamma_0 = 0.8\Gamma_c$ outside the ring, and zero inside. The times of each frame are shown in the lower left hand corner of each, with $t = 0$ being the moment when the ring is lifted. Note the progression of the Marangoni ridge visible in the laser line: soon after the ring has lifted, we see two ridges which soon join to a central distension, which then slowly relaxes. The many bright points in this image are reflective particles which are masked out in the image processing. Data recorded 02/07/14.	38

4.3	Time series of images of a inward spreading data run on a 1.6 mm thick xanthan gum/glycerol mixture fluid layer. Our initial concentration is $\Gamma_0 = 0.8\Gamma_c$ inside the ring, and zero outside. The times of each frame are shown in the lower left hand corner of each, with $t = 0$ denoting the moment when the ring is lifted. Note the progression of the Marangoni ridge visible in the laser line: soon after the ring has lifted, we see two ridges which soon join to a central distension, which then slowly relaxes, just as in the case of the run on glycerol. Data recorded 02/20/14. . . . .	39
4.4	Smoothed height profiles on a 1.6 mm xanthan gum fluid substrate as a function of spatial location in our image, plotted at four different times. Data was taken from an inward spreading run with initial concentration $\Gamma_0 = 0.8\Gamma_c$ outside the ring and no surfactant inside. Data collected on 2/20/14. . . . .	40
4.5	A plot showing measured intensity as a function of radius for two different time values. Results are from inward spreading runs on a 1.6 mm thick layer of a glycerol (4.5a) or xanthan gum (4.5b) with initial surfactant concentration $\Gamma_0 = 0.8\Gamma_c$ outside the ring, and no surfactant inside. . . . .	41
4.6	Fluorescent intensity calibration for NBD-PC on a glycerol fluid layer. Note that the maximum intensity recorded, at $\Gamma = \Gamma_c$ , is approximately half of the maximum intensity seen in 4.5a. Data taken 2/11/2014. . . . .	42
4.7	Radial height and intensity profiles simultaneously plotted as functions of $r$ , for four separate values of $t$ . The smoothed height profile is plotted light green and the intensity profile is dark. Note the correspondence between the location of the height profile at $r = 0$ and and the height of the peak intensity near $r = 1$ . . . . .	43
4.8	Distension height at $r = 0$ and peak Intensity near $r = 1$ as functions of time. Both pieces of data are extracted from an inward spreading experiment on xanthan gum. NB: the lacuna in the data is due to a technical malfunction of the camera. Data taken 2/20/14. . . . .	43

- 4.9 Two images of an inward spreading experiment on a xanthan gum fluid layer with initial concentration  $\Gamma_0 = 0.8\Gamma_c$ . This is taken from an intermediate step of the image processing routine. The image on the left is masked required by the image processing. The image on the right is the same image with the mask removed. Note that the mask does block the spatial extent of the laser line, although it does not block all the light from the laser that is scattered by the xanthan gum. 44
- 4.10 Recorded intensity as a function of radial distance from the center of the ring, plotted at four different values of  $t$ . This data was extracted from an inward spreading run with on a 1.6 mm thick layer of a xanthan gum/glycerol mixture with initial surfactant concentration  $\Gamma_0 = 0.8\Gamma_c$  outside the ring, and no surfactant inside. Importantly, the laser line was off during the collection of this data, so the scattering of the laser by the xanthan gum mixture cannot be corrupting our data here. Note that the recorded intensity values here are much smaller than those in Fig. 4.5b. Data collected 4/10/14. . . . 46
- 4.11 Surfactant Leading Edge behavior for multiple datasets. The leading edge behavior calculated from the experiment on xanthan gum without a laser line is in green, while those manually measured from experiments on glycerol and xanthan gum are in red and blue, respectively. The lacuna in the blue xanthan gum data is again due to a camera malfunction. 47

# List of Tables

- 2.1 Some physical constants pertinent to our system. While  $\rho$  and  $\mu$  are physical constants of the fluid,  $L$  and  $H$  are dependent on the experiments we run.  $L$  is given by the radius of the ring, and  $H$  is given by the height of the fluid layer. . . . 11



# Chapter 1

## Introduction

The study of surfactants and fluid surfaces has a rich history tracing back to Pockels and Rayleigh (1891). This thesis targets the interactions between thin fluid films and surfactants, an area of study for which a comprehensive model arose only relatively recently. Gaver and Grotberg (1990) derived a system of nonlinear fourth order hyperbolic parabolic partial differential equations in surfactant concentration and fluid height profile to model thin fluid film/surfactant monolayer interactions. Since their paper was published, however, few experiments have simultaneously measured fluid height profile and surfactant concentration, although recent experiments from North Carolina State University have proven capable of doing so (Swanson (2010), Strickland et al. (2013)).

We present experimentally determined surfactant behavior as a step towards comparison with a model for surfactant concentration and fluid height profile developed by Gaver and Grotberg. Our goal is to study the spatiotemporal dynamics of surfactant spreading on a variety of thin fluid films. In particular, we study how the surfactant concentration and fluid height profile vary as functions of position and time on viscous Newtonian and non-Newtonian fluid layers.

We begin by motivating the problem and explaining the relevant background for the physical system of interest. We then briefly discuss the model as it pertains to our experimental study. We explain our experimental set-up and protocols on how data is collected. Finally, we discuss results so far and further avenues of interest.



## Chapter 2

# Background

A surfactant is any chemical which reduces the surface tension of a fluid. Surfactants include a wide range of chemicals, with applications ranging from personal care products to industrial cleaners (Hargreaves, 2003). Surfactants also appear in biological systems, such as the human lung. In the lung, oxygen is passed into the blood at sites called alveoli. Alveoli are small sacs kept inflated by the air inside them. The alveoli expand and contract as breathing occurs, although the natural process is hindered by high surface tension. Surface tension of the mucus in the alveoli needs to be quite low. Were surface tension physically dominant, the mucus-covered alveolar walls would collapse, closing off the alveoli and shutting down respiration. In lowering the surface tension, surfactant plays a critical role in human respiration. The surfactant in the lungs is a complicated mixture of many biological compounds, the principal component of which is Dipalmitoylphosphatidylcholine, or DPPC. This surfactant exists as a coating on a thin film of mucus in the alveoli. Once produced in the interior of the lung, DPPC adsorbs onto the mucus film in a monolayer and spreads across the mucus in the alveolus as the lung expands and contracts (Stevens and Sinkin, 2007).

Some premature babies are born with underdeveloped lungs, and are unable to naturally produce DPPC. This deficiency can lead to respiratory distress syndrome (RDS), a common complication of premature birth that is sometimes fatal. RDS can be treated by surfactant replacement therapy (SRT), where a bolus of surfactant is inserted into the babies' lungs. This treatment is often successful, although it is unclear why the treatment fails when it does. It seems clear that the surfactant dynamics of the physical system must apply to this question, although our understanding of the

underlying system is not complete enough to illuminate this application. There are still fundamental questions about surfactant dynamics in even the simplest geometries. It is our hope that studying a simplified version of this system can lead to a better understanding of the system, which may lead to a more efficient or successful treatment if we had more information about conditions that lead to uniform monolayer coating. This example system motivates our study of the simplified problem of surfactant spreading on a thin fluid film.

### 2.1 Our System

The specific system we study is analagous to the surfactant system in the alveolus, albeit in a much simplified geometry. In the alveolus, there are three parts that interact. There is the solid substrate—in the lung, this is the alveolar wall. Atop that is a thin liquid film of mucus which is covered by the third and final part, a monolayer of DPPC. These three elements—substrate, fluid layer, and surfactant—are what form the basis of the surfactant dynamic system in both the alveolus and our experiment. The role of each will be explained below.

#### 2.1.1 Surface Tension

Surface tension is a property of all fluids that arises as a consequence of cohesion. Molecules are inherently cohesive—they prefer to stick together than be pulled apart. Each molecule in a volume of fluid is pulled in by the cohesive force of all its neighbors. In the bulk of the fluid, the tension is equal in all directions, and thus there is no net cohesive force. This can be seen in Fig. 2.1. Molecules on the surface of the volume, however, only have similar molecules on one side. Surface molecules feel some cohesive force from the interior of the volume and not from the exterior. The surface molecules experience a net cohesive force pulling them into the bulk of the fluid. This explains certain physical phenomena, like water forming spherical droplets or small insects being able to walk on water without breaking the surface. Surface tension is a physical property of a fluid, although it can be altered by the application of surfactants.

#### 2.1.2 Surfactant

The common property of surfactants is that they lower the surface tension of a fluid on which they lie. In general, surfactants are part of a

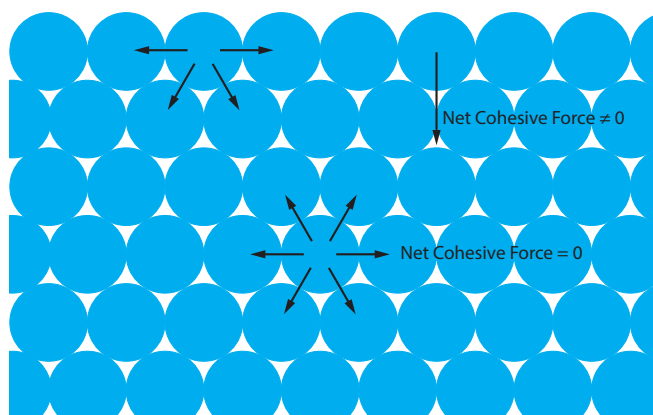


**Figure 2.1** Schematic diagram showing the effect of cohesive forces on molecules in the bulk of a fluid layer and those one the surface. The molecules on the surface feel a net cohesive force pointing inwards. This gives rise to surface tension.

broader class of chemicals referred to as amphiphiles—chemicals that are simultaneously hydrophilic and hydrophobic (Salager, 2002). Effectively, hydrophiles and hydrophobes are molecules that are respectively soluble or not soluble in water or similarly soluble fluids. Surfactants have the common structural property of a polar, hydrophilic head atop a nonpolar, hydrophobic tail. When surfactant forms a surface layer, the hydrophilic head will go into the liquid, while the hydrophobic tail extends up from the surface away from the liquid, as seen in Fig. 2.2. This is an energetically acceptable configuration, as it allows the heads to dissolve into the liquid while the tails do not interact with the liquid. When there is surfactant on the surface, the heads displace water at the surface. The surfactant heads interact more weakly than do the water molecules, and thus the intermolecular attraction at the surface of the liquid, i.e., the surface tension, is considerably weakened by the addition of surfactant.

A certain spatial distribution of surfactant will give rise to spatially varying surface tension. A fluid that has surfactant present only in some area will then have lowered surface tension in that area, and a relatively higher surface tension in an area with no surfactant. Local surface tension  $\sigma$  can be related to the concentration of surfactant,  $\Gamma$ , by an equation of

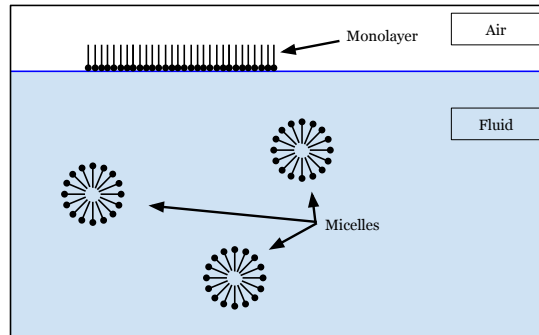


**Figure 2.2** Two possible surfactant behaviors on a fluid. The surfactant molecules at the interface all align with their hydrophilic heads in the water, forming a monolayer. The surfactant molecules can also form spherical micelles, with the hydrophilic heads facing outward and the hydrophobic tails facing inward, which allows the micelle to enter the fluid bulk.

state,  $\sigma(\Gamma)$ . We model the spatial variation of surface tension as a gradient

$$\nabla\sigma(\Gamma) = \frac{\partial\sigma}{\partial\Gamma} \cdot \frac{d\Gamma}{dx}$$

where  $x$  is simply a position variable. This takes into account both spatial variation in the concentration as well as the variation in surface tension due to the concentration of surfactant. Using this, we say that we can model the effect of surfactant as a gradient in surface tension of the fluid. A gradient in the surface tension will create a surface stress known as a Marangoni force, which causes the fluid to move, and the surfactant to advect with the fluid. As the fluid moves, a disturbance in the height profile known as a Marangoni ridge forms near the leading edge of the surfactant. These principles of surface tension gradients and Marangoni forces govern the effect of surfactants on thin fluid films, at least when it comes to surfactant monolayers.

Although we are presently only interested in monolayer behavior, surfactants can also assume other structures. It is important to consider these structures for the simple reason that we want to avoid their formation in our experiment. The surfactant we use is insoluble in our fluid layer. This allows monolayers to form, as the surfactant is held at the surface because it cannot dissolve into the fluid. There is also the possibility of creating a bilayer, which is, as it sounds, effectively two monolayers on top of each other, with the tails of the surfactant molecules mixing. Bilayers, like mono-

layers, are insoluble in the fluid.

There are configurations of molecules which are soluble. For example, surfactants can form micelles, soluble spheres or worm-like strands with the hydrophilic heads on the outer surface and hydrophobic tails in the interior, effectively a monolayer that is closed in on itself. These structures allow the otherwise insoluble surfactant to enter into the bulk of the fluid. Micelles will form if the surfactant concentration is higher than the critical micelle concentration,  $\Gamma_c$ , at which point micelles become an energetically favorable structure as compared to a monolayer. Another structure, similar to the micelle, is the vesicle. The vesicle is also a soluble sphere or worm-like strand, although instead of consisting of a closed monolayer as micelle does, a vesicle consists of a closed bilayer with some fluid inside. This structure also has a surface consisting of the hydrophilic heads of surfactant molecules, so it is soluble as well. We avoid forming all of these structures in our experiment by using an insoluble surfactant at concentrations less than  $\Gamma_c$ .

The particular surfactant we use is 1-palmitoyl-2-12-[(7-nitro-2-1,3-benzoxadiazol-4-yl)amino]dodecanoyl-sn-glycero-3-phosphocholine), also known as NBD-PC. It shares the same hydrophilic head as the lung surfactant DPPC: phosphocholine, hence the PC. A comparison between their molecular structures can be seen in Fig. 2.3. The most apparent difference between them is second tail on the NBD-PC molecule. This tail causes the NBD-PC to absorb light with peak absorbance at 464 nm, and fluoresce with peak emission at 531 nm (ava, 2013). This aspect of NBD-PC is crucial to our experimental design, as discussed in Section 3.

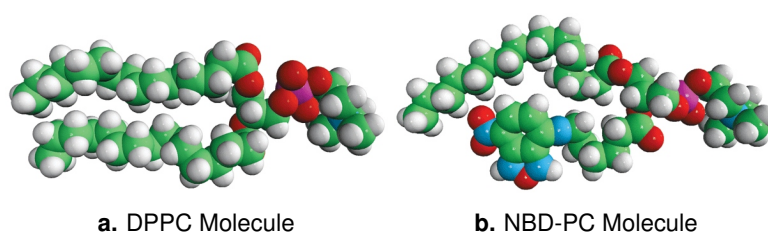


**Figure 2.3** Molecular models of two surfactant molecules. Note the polar heads (the bunched up regions of molecules on the right side of both molecules) and non-polar tails (the long molecular chains on the left side of both) as well as the fluorophore structure on the NBD-PC molecule (this is the ring on the lower tail). Images from Avanti Polar Lipids (ava, 2013)

### 2.1.3 Fluid Layer

The fluid layer in the alveolus is comprised of mucus. Mucus is a complicated non-Newtonian fluid with viscoelastic properties. Non-Newtonian fluids react non-linearly to a linearly increasing strain. Whereas Newtonian fluids, such as glycerol or honey, respond to a stress with a strain proportional to the stress and the viscosity of the fluid, viscoelastic fluids respond with a stress of their own and, after the applied stress is released, return to their original strain state like a spring recompressing after being stretched (Çengel and Cimbala, 2013). This results in more complicated behavior that is much harder to model, and our model cannot account for it. Instead, our model assumes the fluid layer to be a viscous Newtonian fluid, so we perform some of our experiments on a Newtonian fluid layer. We use Sigma Aldrich 99.5% pure glycerol as our Newtonian fluid layer.

Glycerol provides several advantages for our experiments. For one, Glycerol is very viscous, approximately 800 times more so than water at the same temperature. Glycerol's high viscosity causes the timescale of our experiment to be sufficiently slow that we can fully capture the time evolution of the system. In addition, glycerol is very safe, easy to handle, and easy to store, all of which make it attractive from a practical point of view.

Glycerol, though, is still a simple Newtonian fluid, so it does not fully capture the physical behavior of the mucins inside the lung. As such, it is a goal of this experiment to move from glycerol and similar Newtonian fluids to more complicated fluids. Our ultimate interest is to replace the underlying fluid layer with a viscoelastic fluid. That is a goal for both the experimental and theoretical sides of this group. It is considerably more difficult to account for the effects of viscoelasticity in the model than it is to run an experiment with a viscoelastic fluid. Improvements in the model will likely have to be incremental in nature. Presently, the theoretical side of the group is attempting to incorporate shear thinning behavior in the model, as it is mathematically simpler to work with than viscoelastic fluids, although it is still non-Newtonian fluid behavior. Shear thinning fluids respond to an increasing stress with a proportionately higher strain rate. Qualitatively speaking, the fluid responds to a shear by becoming thinner, as the name suggests. The inclusion of shear-thinning fluid is the likely next step forward in terms of the model, and as such, the incorporation of a shear thinning fluid layer in the experiment is our next step forward.

### 2.1.4 Substrate

The final element of the system is the substrate. In the lung, this is the alveolar wall. The wall of the alveolus is bumpy, ciliated, and generally highly non-uniform. Again, though, the lung is merely a related system, and we want to examine extant questions about the fundamental system. It is our interest to understand the basic dynamics of the system at hand. As such, we make the assumption that the substrate is flat and uniform. Thus, in our experiment, we also want the substrate to be flat and uniform in order to permit comparison between the model and experiment. To accomplish this, we use an 8 inch diameter silicon wafer as our substrate.

## 2.2 The Model

The model relies on the assumptions explained above: a thin liquid film; an insoluble surfactant; a Newtonian fluid; and a flat, uniform substrate. The model was first proposed by Gaver and Grotberg (1990). The full derivation of this model is beyond the scope of this thesis, but interested parties can find a rigorous derivation in Swanson (2010) or Kumar (2014). The model originated well before the experimental design explained in this thesis, and, in fact, a desire to test this model drove the original development of the experimental apparatus and procedure described herein.

### 2.2.1 Governing Equations

The model consists of two PDEs which describe the height profile  $h(r, \theta, t)$  of the fluid and the surfactant concentration  $\Gamma(r, \theta, t)$ , as follows:

$$h_t + \nabla \cdot \left( \frac{1}{2} h^2 \nabla \sigma(\Gamma) \right) = \beta \nabla \cdot \left( \frac{1}{3} h^3 \nabla h \right) - \kappa \nabla \cdot \left( \frac{1}{3} h^3 \nabla \Delta h \right) \quad (2.1)$$

$$\Gamma_t + \nabla \cdot (h \Gamma \nabla \sigma(\Gamma)) = \beta \nabla \cdot \left( \frac{1}{3} h^2 \Gamma \nabla h \right) - \kappa \nabla \cdot \left( \frac{1}{3} h^2 \Gamma \nabla \Delta h \right) + \delta \Delta \Gamma. \quad (2.2)$$

where  $\sigma(\Gamma)$  is the equation of state relating surface tension to concentration. The constants  $\beta$ ,  $\kappa$ , and  $\Gamma$  are explained below. From the experimentalist point of view, the variables of interest are  $h$  and  $\Gamma$ , the fluid height and surfactant concentration, respectively. These two variables are what we compare between the experiment and the model, and are thus the variables we want to measure.

We consider these variables to be functions of space and time. Our experimental setup, as explained in the following chapter, lends azimuthal

symmetry to the system. If we consider the system in polar coordinates, then we do not expect variation in  $\theta$ . It is sufficient to specify  $\Gamma$  and  $h$  in terms of radial distance  $r$  and time  $t$ . This is what is meant by the term 'spatiotemporal dynamics:' we wish to capture  $\Gamma(r, t)$  and  $h(r, t)$ .

Equations 2.1-2.2 yield fourth order nonlinear parabolic-hyperbolic system of partial differential equations which are not analytically tractable. Solutions to the system are generally approximated either numerically or with asymptotics. We will not characterize the procedures involved in attempting to produce such solutions. We will discuss certain constant parameters of the system.

### 2.2.2 Important Parameters

In the governing equation, there are three important constants, based on the physical parameters of the system. These parameters indicate which fluid properties should have an impact on the system. The constant  $\beta$  relates gravity and Marangoni forces,  $\kappa$  is the ratio of capillary forces to forces arising from the surface-tension gradient, and  $\delta$  is the ratio of convection to diffusion of the surfactant (Swanson, 2010). The expressions for these are as follows.

- $\beta = \frac{\rho g H^2}{S}$ , where  $\rho$  is the fluid density,  $g$  is the acceleration due to gravity,  $H$  is the characteristic height scale of the problem, and  $S$  is the characteristic surface stress.
- $\kappa = \frac{\gamma H^2}{S L^2}$ , where  $\gamma$  is the surface tension of the fluid film, and  $L$  is the characteristic horizontal length scale.
- $\delta = \frac{\mu D}{S H}$ , where  $\mu$  is the viscosity of the fluid, and  $D$  is a diffusion constant of surfactant.

Some of these constants are known (e.g.  $g$ ,  $\rho$ , or  $\mu$ ), and some, such as  $H$  and  $L$ , depend on the specific geometry of our experimental setup. They are all very specifically derived from fluid properties or the physical setup of the system. Certain of these parameters, such as  $H$  or  $L$ , remain constant through our experimentation, although others, e.g.  $\rho$ , do vary as we experiment on different fluid layers. In order to perform quantitative comparisons with the model, we need accurate measurements of these constants to feed to the numerical simulations. Some of the constants we do have measurements for are found in Table 2.1.

---

Symbol	Constant	Value
$\rho$	Fluid Density	1.25 g/mL (glycerol)
$H$	Characteristic Height	1.6 mm
$L$	Characteristic Length	3 cm
$\mu$	Fluid Viscosity	0.84 Pa·s (glycerol at 25° C) (Segur and Oberstar, 1951)

**Table 2.1** Some physical constants pertinent to our system. While  $\rho$  and  $\mu$  are physical constants of the fluid,  $L$  and  $H$  are dependent on the experiments we run.  $L$  is given by the radius of the ring, and  $H$  is given by the height of the fluid layer.

### 2.2.3 Basis of our Experiment

The main interest of our experiment is the measurement of surfactant concentration and fluid height profile as they evolve in time, so that we may compare these results to those of the model. From this point forward, it is important simply that the reader keep in mind that the variables of interest in the model and experiment are surfactant concentration and fluid height.



## Chapter 3

# The Experiment

Our experiment is motivated particularly by Bull et al. (1999), Swanson (2010), Fallest et al. (2010) and Strickland et al. (2013). Our experimental protocol and apparatus, with some modifications, effectively follows from those presented in Swanson, Fallest et al, and Strickland et al. Bull et al. provide an early attempt at simultaneous measurement of fluid height profile and surfactant concentration by using fluorescent surfactant and fluorescent microspheres to track the fluid profile. Swanson, followed by Fallest et al. and Strickland et al., advanced the technique by using a laser line to measure the fluid profile. This allows one to track the overall fluid profile, whereas Bull et al. were only tracking the location of the fluid disturbance. The experimental methods that we use to measure the surfactant concentration and fluid height come from these sources, especially our collaborators at NC State. In general, we use the fluorescence to track the surfactant concentration and a laser line to measure the fluid height.

### 3.1 The Apparatus

The apparatus we use is visible in Fig. 3.1. We collect all of our data in the form of binary images with a thermoelectrically cooled 14-bit Andor Luca-R camera with 1004x1002 resolution. To provide visual access, the camera is placed vertically above our experimental system. Our experimental system—that is, the substrate, fluid layer, and the surfactant—are contained in an aluminum well. The well is a large, circular piece of machined aluminum with a very uniformly flat circular surface slot of radius  $r = 146.05$  mm. It serves as the vessel for our experiment. When the experiment is being performed, the well holds the 8 inch diameter silicon wafer

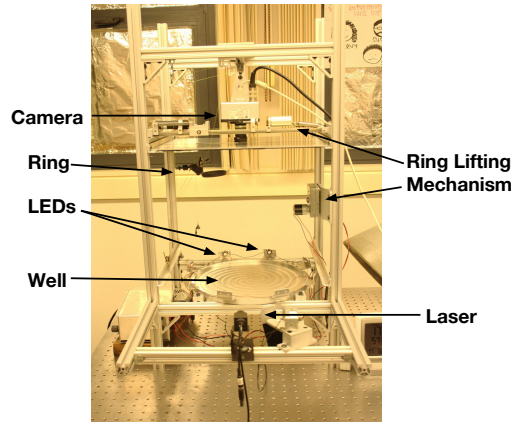


**Figure 3.1** The experimental apparatus in laboratory setting, with major parts labelled. The experimental system is contained by the well where the camera has visual access to it. The LEDs and laser both illuminate the well for the purposes of fluorescence imaging and laser profilometry, respectively. The ring allows us to enforce initial conditions, and the ring lifting mechanism automatically removes the ring when we wish the experiment to start.

that acts as a uniform substrate to the fluid layer, as well as the fluid layer and the layer of surfactant. Evenly spaced around the well are 8 LEDs that provide the illumination for our experiment. The LEDs emit blue light with wavelength centered around 467 nm. This is done specifically to excite the surfactant fluorophore, which has peak absorbance at 464 nm. The NBD-PC fluorophore then emits green light with wavelength centered at 531 nm. To ensure that we see only the surfactant fluorescence and not the LEDs, we block the camera's visual access to the LEDs with an anodized aluminum shield with a central hole 7 inches in diameter and we fit the camera with a Newport Bandpass filter with a  $530 \pm 2$  nm center and a  $10 \pm 2$  nm full width at half-maximum. This enables our use of fluorescence to visualize the surfactant as its position changes in time during an experiment.

To conduct the experiment, we lower a circular anodized stainless steel ring with a 3 cm radius onto the fluid surface to act as a barrier, after which point surfactant is placed outside the ring. The ring lends azimuthal symmetry to our experiment about its center, because the shape of the surfactant begins as an annulus outside the ring. Thus, when we observe the spatiotemporal dynamics of surfactant spreading, we are more specifically interested in the surfactant concentration and the height of the fluid profile

as a function of time and radial distance from the center of the ring. While the ring is in place, the surfactant equilibrates to a uniform height over a period of thirty minutes. We then lift the ring with a motor until it pulls away from the fluid layer and the fluid forms a meniscus around the bottom of the ring. The meniscus is a thin film of fluid which adheres around the bottom of the ring and is pulled up while the ring is raised by the motor. As the ring lifts, the meniscus becomes thinner until it breaks. At this point, a counterweight tips the ring back, triggers a trip wire, and completes a circuit. When the circuit is completed, the ring is quickly pulled by a weighted pulley out of the camera's frame, the LEDs intensify to their brightest setting, and a small shield blocking the laser line drops away. With the ring gone, the surfactant is allowed to spread, and our experiment has begun.

The automation of this experiment is an important improvement over previous iterations. The automation described here garners two main benefits. The automated nature of our experiment ensures greater repeatability, as there is less human interaction with the experiment once it has begun. Additionally, the automation ensures that the total amount of time from meniscus breaking to full collection of valid data takes under one second—usually on the order of a quarter second. This allows us to see earlier time dynamics than other iterations of the experiment, which usually do not have valid data for under one second after meniscus breaking.

There are certain drawbacks to the automation process. Our setup, being more complicated than previous iterations, also tends to break down more often. We lose some amount of lab time to equipment malfunction that we might not if our experiment were simpler and more robust. The specific setup of our experiment is also problematic. For example, the ring does not lower in a straight path, and must be re-aligned with the laser whenever it is lowered. This process is time consuming, and, if performed incorrectly, can jeopardize our data. Despite these drawbacks though, our automated system is a considerable improvement over previous ring-based setups.

### **3.1.1 Improving the Apparatus**

Changing the apparatus with an eye towards making it more reliable and capable of producing repeatable experiments is an ongoing goal of this research. Over the course of the year we have made certain improvements and have some plans for others.

### The Shield

One main aspect of the experimental apparatus on which we have improved is the shield. Originally, the shield's central hole was 8 inches in diameter, equal to that of the wafer. Since the shield is closer to the camera than the wafer, the image of the shield-hole was larger than the image of the wafer. Thus, no matter where the shield was positioned relative to the wafer, some amount of the well was visible. Since the well scatters the incident LED light, the visible section of the well saturated the CCD element in the camera, which not only damages the camera, but also makes any data in that region unusable.

We had a shield machined with a central hole 7 inches in diameter and made of the same thickness of aluminum as the previous shield, and we painted it black to minimize reflection. This resulted in less visible area, although it did not fully exclude visibility of the well. Additionally, the new shield is slightly smaller than the original, and thus fit less tightly in the framework. This allowed us to adjust the location of the shield slightly. When putting the new shield in place, we disturb the apparatus less, because we have to use less force to place it. When placing the older shield, the experimenter would have to strongly force it into place, which tended to cause dust to fall into the well. By making the shield smaller, we have successfully avoided this problem.

### The Well and LED Circuit

The circuit which governs the behavior of the LEDs is of paramount importance to the functioning of our experiment. If the system does not trigger when the meniscus breaks, then we lose precious seconds at the very beginning of the experimental run, and often completely lose sight of the phenomena which happen at faster timescales in this problem. This circuit suffered two problems at the beginning of this semester. The first problem lay in the LEDs' connections. The LEDs, which are fixed to the well, are connected in series by loose wires soldered to contacts on each LED. Members of the lab giving the well a rigorous washing often accidentally broke the solder joints connecting the LED wires. This required us to finish washing the well, resolder the wire, and then wash the well again in case the process of soldering dirtied the well. If the solder joint was good and the circuit worked—i.e., at best—this was a nuisance. At worst, the solder would not be good, and the circuit would not work at all, foiling any attempt to collect data. By a certain point, the well's solder joints were so

messy that we took the measure of removing all the wires and resoldering from scratch. However, we did not do a very good job, and the well circuit remained non-operational. At this point, we sent the well to Walter Cook to be resoldered. He not only fixed the solderings, but also routed the wires around the edges of the well. After that point in late January, the LED circuit (not including the tripping mechanism) worked reliably, and only one solder joint has been broken since Walter Cook's intervention.

Although the well has been more robust and failed less often in the Spring, it has still failed more than once, each instance of which owed to the act of moving the well and handling the LED circuit roughly. An assembly which does not require handling the circuit to change out the well would likely be much more reliable. This could be as simple as affixing the LED circuit to the 8020 framework so that the LEDs are stationary. This improvement would make the apparatus less prone to failure and thus conserve lab time. Additionally, if the LEDs are affixed to the framework and not the well, we can allow for the possibilities of using multiple wells, which could also save a good deal of lab time.

### **The Ring Circuit**

The second part of our circuit, the ring tripping mechanism, also proved problematic at times. In perfect operation, the ring will tilt back when the meniscus breaks and contact a wire with its front edge, thus completing a circuit which not only brightens the LEDs, but also drives two solenoids, one of which reveals the laser line, the other of which causes the ring to lift out of the frame. In practice, though, we often saw the ring make contact but fail to trigger. Again, Walter came to our aid. He noted that the black oxide coating on the ring, which we use to ensure its reflection isn't visible in the image, is non-conductive. After scraping just the top outside edge of the ring to remove some of the coating, we found that the triggering mechanism worked precisely as intended. After we fixed these two issues with the circuit, the automated part of our apparatus worked nearly flawlessly, and enabled us to gather valuable quantitative data for the first time in our lab.

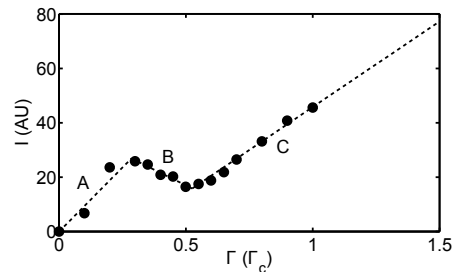


**Figure 3.2** Fluorescence intensity vs surfactant concentration as a fraction of the critical micelle concentration  $\Gamma_c$ . Note the non-monotonic but piecewise linear shape. Figure taken from Strickland et al. (2013).

## 3.2 Measuring Variables of Interest

### 3.2.1 Surfactant Concentration

The use of fluorescence to track the spatial evolution of surfactant in time originates with Bull et al. (1999). They used surfactant fluorescence to track the movement of the leading edge of surfactant, but did not study the concentration of the surfactant over their system. While the leading edge behavior is certainly of interest, we want to study the total concentration field of the surfactant rather than just the location of the leading edge, which Bull et al. do not report. Fallest et al. provide a method of determining the concentration of the NBD-PC from the intensity of the fluorescent response under illumination (Fallest et al., 2010).

In order to determine the concentration from the intensity, we must first find a direct relationship between the two. To do this, we can deposit a known concentration of surfactant on the fluid layer, illuminate it with the LEDs, and image to record the fluorescent intensity. We can construct a relationship between fluorescence intensity and surfactant concentration by repeating this process for a range of surfactant concentration. The result of such a calibration can be seen in Fig. 3.2 (Strickland et al., 2013)

It is important to note that the relationship between fluorescent intensity and surfactant concentration is non-monotonic. The fact that it is non-monotonic means that the relationship is not simply invertible. In a range of  $0.3\Gamma_c < \Gamma < 0.7\Gamma_c$ , the intensity of fluorescence as a function of concentration is multivalued, and thus we cannot easily deduce the concentration from the fluorescence intensity. Previous work has established an approach assuming the continuity of surfactant concentration and taking advantage

of the piecewise linear form of the relationship (Strickland et al., 2013).

The non-monotonic relationship between fluorescence intensity and concentration is due to fluorescent resonant energy transfer (FRET) effects (Shrive et al., 1995). FRET occurs when an excited fluorophore transfers energy to a nearby fluorescent molecule, moving from the excited state to the unexcited state without fluorescing (Selvin, 2000). The prevalence of FRET is highly dependent on the proximity of fluorophore molecules—if the concentration is high, then FRET will be very important to the system. In effect, if the fluorophore concentration is too high, then some amount of excited fluorophores will not fluoresce because of FRET. Hence, the plot of intensity versus surfactant concentration is non-monotonic.

We suspect that we can avoid FRET by using a mixture of NBD-PC and non-fluorescent surfactant such as POPC or DHPE, which can keep the concentration of fluorophores small for any concentration of surfactant. This is a future avenue of our project, as it would make the measurement of surfactant concentration from fluorescent intensity much easier.

### 3.2.2 Fluid Layer Height

To determine our fluid height profile, we use a technique known as laser profilometry. We use a Laserglow Technologies Brightline Pro 20 mW 532nm laser with a fanning angle of  $100^\circ$ . The laser's beam forms a triangular sheet, which intersects the fluid layer along a line. This beam line is what we see on the camera. As the light comes out in a triangular plane, the height in the  $z$ -direction of this intersection line is a linear function of the distance from the laser. Thus, a point in this plane slightly closer to the laser will have a slightly greater height. The simple mechanics of this can be seen in Fig. 3.3

If the fluid layer is flat, the intersection between the fluid layer and the laser sheet is a straight line. The location of the line in the plane of the well, and thus in the image our camera sees, is dependent on the height of the fluid, and therefore disturbances in height profile will appear as disturbances in the shape of the laser line. This method allows us to track the fluid height profile as it varies over the system.

As we are interested in the fluid height as a function of radial distance, we need to ensure that the laser line passes through the point about which we have azimuthal symmetry, i.e. the center of the ring. To do so, we lower the ring until it is just above the uniform fluid surface. Then we adjust the angle of the laser until the line just hits the bottom of the side of the ring closer the laser, then reflects off of the wafer, and then hits the very bottom

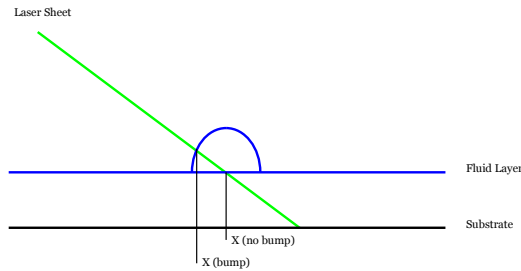


**Figure 3.3** Schematic of laser line mechanism. Because the laser sheet is flat, the location of its intersection with the fluid is linearly related to the height of the fluid layer.

of the side of the ring further from the laser. Based on the geometry of our experiment, this means that the angle of the laser is aligned such that the laser line passes through the center of the ring. This geometry can be seen in Fig. 3.4

Once the laser is aligned, we also need to determine the relationship between laser position and fluid height. By the geometry of the interaction, we know the relationship is linear, although we need to exactly specify it. We do so by first aligning the laser at a certain height, typically 1.2 mm, and take an image. Then, we add more fluid in increments of 0.2 mm and record images at each level. We can note the change in distance of the laser line as the height increases. This allows us to determine the exact relationship between laser line position and fluid height, so that we can use laser profilometry to measure the fluid height. It is worth noting that the relationship between height and location is not perfectly linear, as our camera has a fisheye lens which distorts the image. However, the image is distorted by such a small amount that we generally make the approximation that the relationship is linear.

Once we have properly calibrated the laser, we can begin to run our actual experiment. We will now discuss how an experiment is set up and run.

### 3.3 Laboratory Methods

The goal of all of the protocols of our labwork is the repeatability of our experiment. A small difference in the experiment could produce divergent

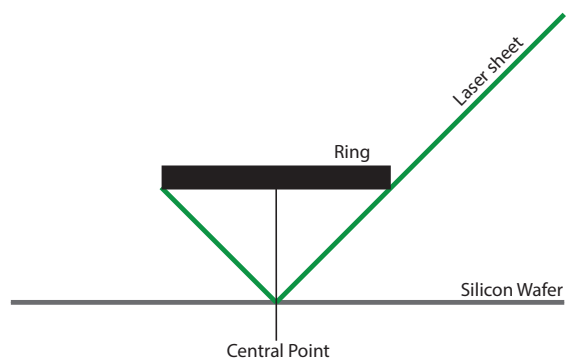


**Figure 3.4** A schematic diagram showing the geometry involved in aligning the laser. By that the laser sheet hits the ring at the same point on both the front and back edge, we can geometrically ensure that the laser hits the substrate along the diameter of the ring.

results as our experiments involve surface effects for which the governing equations are highly nonlinear. We must therefore be very stringent about maintaining consistency across experiments and multiple researchers.

### 3.3.1 Pre-Experiment Protocols

First, we must take care to properly clean and handle our apparatus. Before an experiment can be run, we must thoroughly wash every part of our experiment that touches the liquid to be used. We wash the well once with detergent and deionized water. For the wafer, we subject it to an UV-ozone cleaner. Finally, all glassware (beakers, glass syringe, etc.) are soaked in a Contrad-70 solution. Before any contact with the fluid of the experiment, everything - glassware, well, and wafer—is rinsed with 18 M $\Omega$  water and dried with nitrogen gas. In addition, all equipment is handled with gloves with exception of the silicon wafers which are handled with specialized tongs so as to not change the surface chemistry of the wafer. This extensive cleaning protocol is to ensure that our experimental apparatus is as uniform as possible across experiments.

In addition, we have protocols in place for creating the fluid mixture that will serve as the thin film. The glycerine we use is 99.5% pure from Sigma Aldrich, and is used as it is prepared by Sigma Aldrich. The 0.5% xanthan gum mixture we use is prepared between 24 and 48 hours in ad-

vance. We use an IKA RW 20 Digital propeller mixer to prepare the solution, taking care to mix at a rate of 60 rpm in order to not disrupt the fluid properties of the xanthan gum mixture. We first mix the xanthan gum, which comes in a pure powdered form from Sigma Aldrich, into glycerine for two to four hours. Then, we add an equal mass of epsom salt to be mixed in over the course of two to four more hours, as suggested by Ciullo and Flynn (2000). We add enough xanthan gum powder to create a mixture that is 0.5% by weight xanthan gum, 0.5% by weight epsom salt, and 99% by weight glycerol. Once the mixing is complete, we place the mixture in a refrigerator overnight to inhibit bacterial growth.

Once we need to deposit the fluid layer, we use a 20 mL glass syringe to transfer it from the container to the well. We first wash the syringe as is dictated by our protocols, then we wet the plunger of the syringe with the fluid to be deposited as lubrication. Then we deposit the fluid in the well measuring to the mL, as the volume of the fluid deposited will correspond to the height of the film it forms. Once we deposit the fluid, the film it forms will not be a uniform thickness over the whole well.

We need a uniform surface, so we wait for the fluid layer to disperse itself in the well and become uniform. In general, this takes one to two hours. Once the fluid layer has settled, we can apply the surfactant. Before that, we take background images of just the fluid layer under LED illumination. Then, we lower the ring into place, and deposit our surfactant. While our apparatus allows us to study both outward spreading surfactant (in which the initial surfactant is deposited on the interior of the ring) and inward spreading surfactant, we focus on the latter case in our experiments.

Our experiment is concerned with inward spreading of surfactant, although the setup procedures for the two are very similar. For outward spreading the surfactant is deposited inside of the ring at the beginning, and for the inward spreading, the surfactant is deposited outside the ring. After that point, though, the two types of experiments are run the same way. After depositing the surfactant, we let it equilibrate for half an hour once it has been deposited. The surfactant forms a uniform coating while the chloroform in which the NBD-PC is dissolved evaporates away. While the chloroform evaporates, the lab is briefly vacated as a safety precaution while a snorkel hood placed close to the experiment clears out the chloroform vapor. After this, we are able to begin our experiment.

After the surfactant has equilibrated, we simultaneously begin taking pictures at a rate of approximately 3 Hz and start the ring lifting mechanism. Then, the experiments proceed as described previously, and we collect our images. In order to extract meaningful data from these images, we

need to apply image processing techniques.

## 3.4 Image Processing

The image processing suite is written in MATLAB, and can be broken down into two distinct branches. As we are trying to measure two variables of interest—the surfactant concentration and the fluid height profile—we have separate codebases for each. I will first explain the code that calculates the fluorescence intensity, and then the laser line processing.

Our experiment exhibits azimuthal symmetry, and therefore we expect the behavior of our system to be a function of solely radius and time. The symmetry of this problem arises from the initial conditions. The surfactant begins as an annulus spreading inward. The shape of both the area covered with surfactant and the voided area that the surfactant spreads into are rotationally symmetric. In fact, they are both symmetric about the same point: the center of the ring. We can find the center of the ring, and thus the point about which we have azimuthal symmetry. Using this, we can categorize the system's behavior as a function of radius. We first find the intensity of the fluorescent surfactant as a function of radius.

### 3.4.1 Intensity as a Function of Radius

To facilitate some ease of use, we have a single MATLAB function to analyze a full data run and produce a time series of plots of intensity versus radius. The intensity measured is the brightness value of the pixels of the images, which is ideally caused by surfactant fluorescence, although it can be caused by other external factors (e.g. a speck of dust illuminated by our LEDs or a stray reflection). We need to apply this processing to the intensity values of the image because ultimately, the intensity is the only thing we can measure with our camera.

We first need to know exactly how to run that function, though. To determine some of the appropriate parameters, like which areas of the images to remove from the analysis and which area of the image is of interest to us, we need to get a good look at the actual images of the run. For that, we use some preliminary functions to view the data run itself. Then, to find the intensity as a function of radius, we first perform relatively simple background subtraction on our data images. The background subtraction process simply aims to find a representative background signal and remove that from our data images so that we especially see the details of interest

which are not present in the background. This requires us to find an appropriate background signal, which we construct by averaging and smoothing multiple background images. After that, for our analysis to continue, we must find the point about which we have azimuthal symmetry, from which the radial distance can be measured. Finally, once we have that information, we can azimuthally average the intensity data and produce plots of intensity as a function of radius.

### **Preliminary Functions**

Our preliminary functions allow us to convert the arrays of intensity values recorded by the camera back into images. In order to perform the full image analysis, we need to know certain parameters about the dataset. Importantly, we need to know what parts of the image are important to the analysis, which parts to mask out, and at what frame the real data begins (i.e. at what frame the ring breaks contact with the fluid). In our image processing, we only analyze a small subset of the image. We do this because it is computationally much less expensive to work with a smaller image, and we are chiefly concerned with what happens in the neighborhood of the ring. We also have to do some masking in order to reduce systematic error—for example, counting the intensity of the laser line in surfactant fluorescence intensity calculation would produce significantly higher intensity values than what we would really expect. Finally, the function which calculates intensity as a function of radius also requires the point at which the ring breaks contact, in order to have a frame in which the ring is in place so that it can find the center of the ring. To figure out all of this information, we need to be able to look at the data as it appears in MATLAB.

We use a function called `viewRun` to do so. This function is told where to find the data and background images, which frames to start and end at, and how quickly to display each frame. It performs a very simple background subtraction on each of the data images it is given and displays them. When it displays the images, it uses a technique known as thresholding, wherein all the intensities in the image above or below certain thresholds are rounded to their respective high or low thresholds. Determining these thresholds is a heuristic process. The purpose of this function is to display the raw images in such a way that their salient features are easiest to see by eye, so thresholding is fundamentally determined by preference. It's worth noting that the act of thresholding does not affect or change the data in any way, it only alters the displayed data. This alteration allows for full contrast in a region of interest of intensities that makes the images

easier to see.

Once we have the information we need from this part of the analysis, we can begin the process of image processing proper. The first part of our image processing suite involves background subtraction of a slightly more sophisticated variety than that above. Instead of simply subtracting one image from another, we create an average, smoothed background in order to eliminate the effect of random noise in any one of the background images. After that, we find the point about which we have azimuthal symmetry in the problem. To do this, we use an edge finding algorithm called the Hough transform. In both of these processes, a common technique called convolution is used.

### **Convolution: Gaussian Smoothing and the Hough Transform**

Convolution is an important tool in image processing. Convolution involves using two images or matrices (in the context of our image processing in MATLAB, the images are matrices), the input and the kernel. The process of convolution proceeds as follows. For each pixel in the image, we align the image matrix and the kernel matrix such that the center of the kernel is aligned with the selected pixel. Then, each pixel in the image is multiplied with the pixel of the kernel 'above' it, and all of the resultant products are added together. The sum is then normalized by a norm specific to the kernel being used and inserted into the new convoluted image at the location of the pixel in the original image. We then move onto a new pixel in the image, shifting the kernel above the image so that the center of the kernel is aligned with the new pixel of interest. One can think of the kernel sliding over the image, with the center of the kernel always aligned with a particular pixel in the image. This process is repeated for each pixel in the input image, and we construct the convoluted image one pixel at a time.

The specific structure of the kernel governs what the convolution does. There are two places where we use convolution in our image processing. We use convolution in the Gaussian smoothing process, as well as in the Hough Transform.

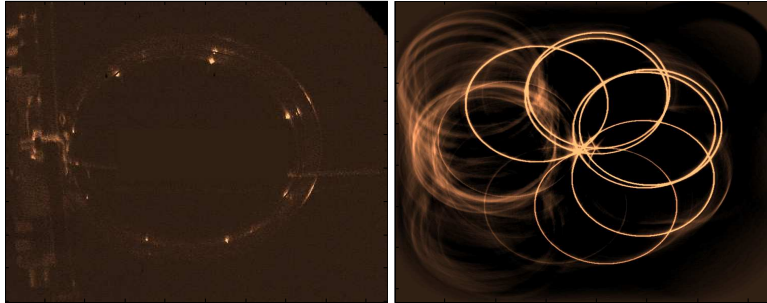
One of the first steps in our image processing is background subtraction, and one of the first things we do in background subtraction is Gaussian smoothing. We expect the pixels in our background images to have some amount of random noise in their intensity. However, we are trying, through the process of background subtraction, to remove any systematic intensity fluctuations, and not introduce random noise into our data. As

such, we use smoothing to reduce the noise in the background images. In general, a smoothing algorithm will take the intensity value of a pixel and average it with the intensity values of its neighbors. The main assumption of this technique is that any pixel will look very similar to its nearest neighbors, except for the effect of random noise. Depending on the amount of variation one is willing to tolerate, different weightings can be applied to the averaging process.

As suggested by the name, the Gaussian smoothing process uses a Gaussian weighted average. To calculate this average, we create a matrix with each cell corresponding to a different point in a two-dimension Gaussian. This matrix is then used as the kernel in a convolution with the image to be smoothed. With the center, that is, the peak, of the Gaussian aligned above a pixel, the convolution process multiplies every pixel in the image with the value of a point in the Gaussian, adds them all up, and stuffs the result into the pixel of interest into the convolved image. In this way, this kernel provides a Gaussian weighted average of a pixel's intensity with those of all of its neighbors when convolved with an image. This allows us to reduce the random noise in our background image, and find something closer to the systematic background offset.

Gaussian smoothing is merely the product of using convolution with this specific kernel. Again, using a different kernel produces a different effect. This is what allows us to also use convolution for the Hough transform.

In the Hough Transform, the kernel we use is a circular mask. That is, the kernel is a matrix with a circular arrangement of ones, and zeros everywhere else. We use this kernel because we're looking specifically for a circle in the image. Consider an ideal case, where the image is simply a high-intensity circle, and dark everywhere inside and outside the circle. When the center of the kernel is aligned with the center of the circle we seek, the bright circular image lines up with the circular mask. This maximizes the resultant sum of products of the corresponding kernel and image pixels. Thus, the pixel in the convoluted image at the location of the center pixel in the input image will have a large value. Specifically, because the kernel here is unweighted, the value is equal to the sum of all the intensities of the pixels in the image of the circle (assuming each pixel is matched to a nonzero pixel in the kernel). However, all the pixels around the center point, whose magnitudes are calculated by centering the kernel above them, will have small values—the circular kernel will only intersect with the circular image in two points. In that case, the value of the convoluted image at that point will be equal to the sum of the intensities of the two



**a.** Image to be convolved with a circular kernel. **b.** Image produced by convolution of 3.5a with a circular kernel

**Figure 3.5** The image of our ring before and after convolution. Note the locations of the bright spots in 3.5a, which correspond to the centers of the bright circles in 3.5b. The center of our ring, as found by the Hough Transform, is the bright point at the center of the image where the circles intersect.

points of intersection between the two circles. If the image is of a circle, then the point that maximizes intensity in the convoluted image is the point where the two circles' centers align—that is, the center of the circle in the input image. Thus, using this kernel, a circle in the image is transformed into a point in the convoluted image.

The converse is also true: a bright point in the real image is transformed into a circle in the convoluted image. This is relatively easy to see, as the maximum brightness occurs when the circular kernel intersects with the bright point. This occurs whenever the center of the kernel is aligned with a pixel that is exactly one radius away from the bright point. This means that, for all points exactly one radius away from the bright point, the convoluted image has a bright point. Thus, a circular kernel convolved with a bright point will produce a circle in the resultant image. Thus circles in images become transformed into points, and points become transformed into circles when convolved with a circular kernel. This is visible in Fig. 3.5.

The figure shows both a real image of our ring set up, already cropped and masked, and the resultant image transformed by convolution with a circular kernel. Each of the bright points in the real image corresponds to the center of a circle in the transformed image. Because each of the circles has a radius equal to that of the ring and the points about which they are centered are located around the edge of the ring, the intersection between all the circles must be the center of the circle.

There is one more important aspect of the Hough transform algorithm.

The Hough Transform works with a voting method; it performs the convolution for many kernels with circles of different radii and calculates the maximum intensity of the convoluted image for each kernel and keeps track of the global maximum intensity over all kernels. The kernel that produces this maximum will be a circle of the correct radius, and the location of this maximum in the convoluted image will be the center of the circle in the input image.

One final point of interest with regard to convolution is the process by which MATLAB performs it. It is a common fact of Fourier analysis that convolution in the original domain is equivalent to multiplication in the Fourier domain. Thus, it is equivalent to take the two dimensional Fourier transform of the two images, multiply them, and take the reverse transform of the product or to simply do the convolution. MATLAB's Fast Fourier Transform algorithm is faster than simple convolution, so performing the FFT confers benefits over simple convolution. In fact, this is the way that MATLAB performs convolution.

### **Azimuthal Averaging**

The final step of our image processing involves extracting fluorescent intensity data from our images. We want to find the intensity at specific values of radial distance. Since we take two dimensional images, we have multiple values of intensity over arcs of constant radius (i.e. circles). We use this to our advantage by averaging the values of intensity over these arcs. This technique is known as azimuthal averaging.

Azimuthal averaging provides better statistics, more accurate data, and protection from perturbative effects like fingering. Because we are averaging over many pixel intensities, we can find robust statistical averages with only a single experimental run. Further, these averages more accurately reflect the intensity of the surfactant and are less susceptible to random fluctuations. There are also non-random fluctuations whose effects can be mitigated by azimuthal averaging. One such effect is fingering, where the leading edge of the surfactant forms fingers, and no longer expands in a circle (Troian et al., 1989). The azimuthal averaging scheme can account for this by essentially smoothing over any fingering instability in our data. Azimuthal averaging is a very useful technique that provides a way to reduce error, both random and not, in our data.

There is one important drawback to azimuthal averaging and radial binning. The number of data points for us to average over at a radius  $r$  is effectively the size of a circle with that radius. The number of data points

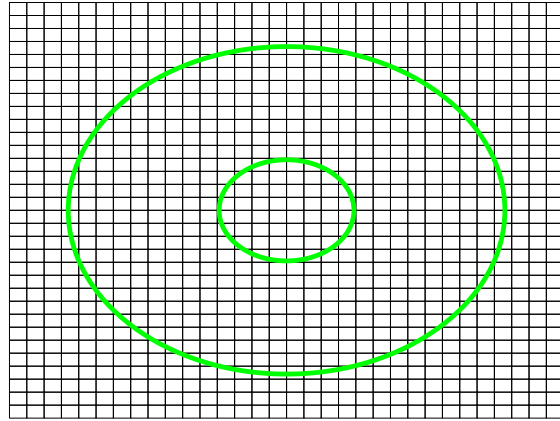


**Figure 3.6** An schematic showing the dependence of sample size on radius using an azimuthal averaging scheme. The larger circle passes through more bins than the smaller, thus it will be averaged over a larger sample size.

is proportional to the circumference of the circle, and thus to the radius. This is visible in 3.6. Note the significantly larger number of bins passed through the larger circle. One can see also that, if a circle were large enough, it would pass only through the corners of the matrix. In cases where the radius is rather small or very large, the number of bins covered by the signal is small. For circles with small or large enough radius, the statistics are not good enough to account for noise. This means that data either too close to the center or too close to the edge has to be masked out. This is one disadvantage to azimuthal averaging.

After the Hough transform has been performed and we have located the center of the system, we can begin binning pixels based on their radial distance from that point and averaging the values of intensity in those bins. With that, we can extract our fluorescent intensity data as a function of radius and then, using the calibration mentioned above, back out our surfactant concentration as a function of radius.

### 3.4.2 Processing the Laser Image

In addition to the intensity of surfactant fluorescence, we also need to extract the height of the fluid layer from our images. Because of our calibration of laser location to fluid height, this is relatively easy. We can find the location of the fluid based simply on the location of the laser line. Where

the laser line moves off of its baseline in the images—as measured by the laser position at the edges—we can determine from its movement in the plane of the image the height of the fluid in that location. We can do this over the length of the laser line to determine the fluid height at any moment as a function of position.

### **Finding the Laser Line**

The key first step in the height profile analysis is locating the position laser line in the image. Heuristically, this is quite simple—the laser line is visible as the bright line in the image. One can point out immediately by eye where the laser is—it is the intensely bright line across the image. Our image processing works in a similar manner, by looking at the overall intensity of the images. It is more complicated than simply finding the brightest point in the image.

We first select the part of the image with the laser line in it, so that we need not waste computer time by considering parts of the image with no laser in them. Then we slice this smaller image into vertical slices corresponding to the columns of pixels in the image. For each column, we take the fourth power of the intensity of each pixel, multiply that value by the pixel index, sum this product over the whole vector and normalize by the sum of the fourth powered intensities in the column. This is effectively a weighted average that gives us the index value of the laser line. The use of the fourth power in this algorithm was reached based on some experimentation, rather than based on a priori mathematical rigor, although it appears to work well at matching the laser line, as can be seen in Fig. 3.7, which shows three snapshots in time of the image of the laser line with the calculated laser line superimposed. This approach is viable because the laser line is significantly brighter than anything else in the images.

We are interested in not just the location of the laser line, though, but in its perturbation from the straight line. We must find, then, the straight line at equilibrium. We do this by using reference images of the flat laser line taken before the surfactant has been deposited, or if those are not available, we use images of the laser line in the long time limit, usually taken on the order of 10 minutes after the ring has lifted; by this point the laser line has fully reached equilibrium and can be treated as flat, although the use of a reference image is preferable.

We find the flat line the same way we find the laser line, using the weighted average process on the reference image. This process creates relatively noisy data that we then must smooth. We smooth the data using a

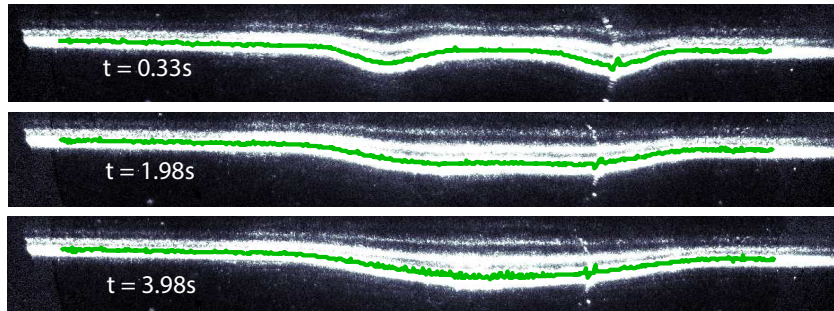


**Figure 3.7** Calculated laser line in greensuperimposed on an image of the laser line at three moments in time.

moving average, where we replace each point with the mean value of all the points in a span centered around this point. This makes the noise much less distinct, but it also reduces other important features. Spatial averaging will reduce the apparent height of the peaks, for example, by averaging the peak point with a large set of points which are of smaller magnitude. The larger the span, the more pronounced this effect. Thus, the choice of span is critical to how accurate our smoothed data is. One can see this in Fig. 3.8, where the smoothed data (seen in red) becomes less responsive to the noise (one sees this especially in the flat wings) but the peaks of the smoothed data become noticeably lower than the peaks of the noisy data. Based on what is seen in that image, we choose a span size of 20 data points for the purpose of smoothing, as that appears to maintain the values of the peaks while providing ample noise smoothing.

Once we have the flat line, we simply subtract that from the measured laser line location—this gives us the perturbation from flat of the laser line, which we then convert from pixels to centimeters in order to have a measure of the fluid height profile. We find the ratio of pixels to centimeters by performing a laser line calibration measurement, which requires us to take reference pictures at different, known fluid heights in order to determine how an exact change in height corresponds to a horizontal shift in the laser line. For our experiments, this ratio was found to be  $4.9 \pm 0.3$  pixels to the centimeter.

We would also like to find the height profile as a function of radial distance. While our code does not as yet have this capability, it is not conceptually difficult to imagine how it may be implemented. We would simply find the center of the ring using the Hough transform, then split the laser

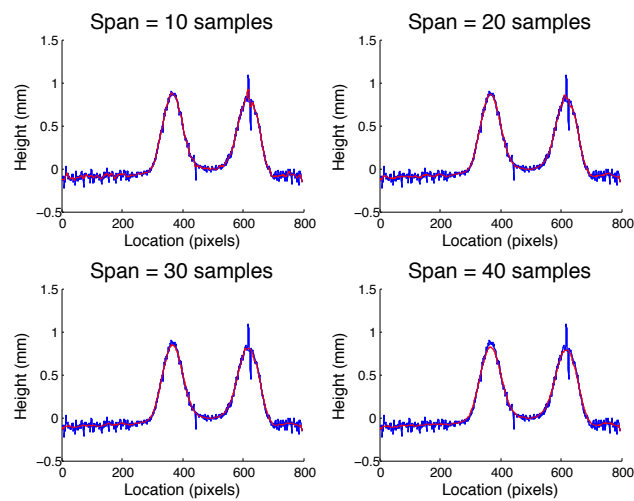


**Figure 3.8** Four spatially averaged height profile datasets superimposed on the noisy data, with varying size of span. As the sample size increases, the spatially averaged data (in red) becomes less noisy, as visible especially in the flat wings of the dataset, but the significant differences (i.e. the peaks) also begin to get smoothed out at some point.

line about this point into the right and left sides, and thus we would obtain a dataset for height profile as a function of radial distance. This would be the final step of our process for the extraction of height profile data from our images.



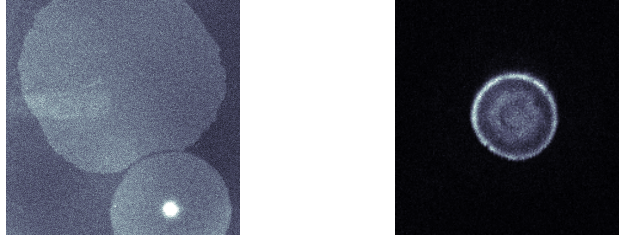
# Chapter 4

## Results

We have outlined how we collect data; now we will present the data we collected over the previous semester. We conducted inward spreading surfactant experiments on 1.6 mm fluid layers consisting of either glycerol or a xanthan-gum glycerol mixture. We extracted intensity profiles as a function of radial distance from the center of the experiment for both fluid layers, and height profiles as a function of spatial position in our image for the xanthan gum fluid layer. The intensity profiles we extracted seemed contrary to what might reasonably be expected, although a few other measurements revealed them to be more or less a typical intensity profile that had been obscured by the interference of the laser line for small  $r$ . Even given this interference, we are able to extract some information about the behavior of the leading edge of surfactant on a xanthan gum fluid layer, a novel result.

### 4.1 A New Fluid Layer

One of the main goals of this research was to perform surfactant spreading experiments on a shear-thinning fluid layer. To do so, we first had to identify a shear-thinning fluid. Once we identified such a fluid, we had to consider how we might produce it in the lab, then test if the fluid as we had produced it would be viable for our experiments, that is, if it would allow for visualizing both the laser line and the surfactant. Suspensions of xanthan gum appeared frequently in the literature as shear-thinning fluids, so we elected to try them as our fluid.



**a.** Two surfactant droplets visible on a glycerol fluid layer      **b.** A surfactant droplet visible on a xanthan gum suspension fluid layer

**Figure 4.1** Surfactant droplets visible on different fluid layers

#### 4.1.1 Introducing A Shear Thinning Fluid

Xanthan gum suspensions are well studied fluids that exhibit shear-thinning properties (Song et al. (2006), Zhong et al. (2013)). As such, we chose to use a xanthan gum suspension as our shear-thinning fluid. We initially tried a suspension of Xanthan Gum in 18 M $\Omega$  water. When we placed this suspension into the well and deposited a surfactant droplet onto it, the droplet was visible only at first while it was limited in spatial extent, and thus at high concentrations. When the droplet began to spread outward and the local concentrations decreased, we could no longer visualize the surfactant. At this point, we considered suspending xanthan gum in glycerol, because we had previously been able to visualize surfactant on glycerol. Using the mixture specified in the previous chapter, we were able to image surfactant, as can be seen in Fig. 4.1b. For comparison, we have a picture of two surfactant droplets on a glycerol fluid layer, as visible in Fig. 4.1a. We were not able to image surfactant on a water-xanthan gum fluid mixture.

We use a specific mixture of xanthan gum, epsom salt, and glycerol because of results reported by Ciullo and Flynn (2000). They report the flow index of xanthan gum dissolved in glycerol and water in multiple concentrations. The flow index measures the pseudoplasticity of the fluid, such that a lower flow index means a greater shear-thinning effect. A 0.5% mixture of xanthan gum in water has a flow index of  $n = 0.33$ . The same concentration in glycerol has a flow index of  $n = 0.47$ . By adding 0.5% epsom salt, the flow index increases to 0.54, although the yield stress and viscosity both decrease, making the fluid easier for the surfactant to shear. The xanthan gum mixture we use is shear thinning, and as can be seen in

Fig. 4.1, we can image surfactant on this fluid layer. We are now able to perform our full inward-spreading experiment on a shear-thinning fluid layer.

## 4.2 Hole Closure on Glycerol and Xanthan Gum

### 4.2.1 Experimental Images

While experimentation with xanthan gum fluid layers was one of main goals of our research, we were also simultaneously attempting to recreate results that had previously been seen at North Carolina State University. While our lab was running similar experiments over the summer, some technical difficulties rendered this data unusable (to be exact, the camera's exposure setting was too low, so we could not properly observe the surfactant fluorescence). At the beginning of this semester, we did not have tangible results to show for our many efforts. Our first interest in conducting experiments was in attempting to find results similar to those of the NCState group using glycerol as a fluid layer. Figure 4.2 shows one such experiment.

This run is an inward spreading (or hole closure) experiment using a 1.6 mm thick layer of glycerol as a fluid layer, with an initial concentration of  $\Gamma_0 = 0.8\Gamma_c$  outside the ring, and no surfactant inside the ring. The times, listed on each frame in the image, are relative to the moment when the ring lifts, denoted as  $t = 0$ . Note that, after the ring lifts, two ridges are visible at the edge of the hole with little surfactant. As the hole closes in a matter of seconds, the two Marangoni ridges come together to form a single central distension. This central distension relaxes, but much more slowly than it was formed. Physically, this makes sense, because the concentration gradient is much larger between the hole and the outside region than it is after the hole has been filled.

We also performed full inward spreading experiments on non-Newtonian shear thinning fluid layers. Such an experiment on xanthan gum can be seen in Fig. 4.3. This is an inward spreading run on a 1.6 mm thick xanthan gum fluid layer with  $\Gamma_0 = 0.8\Gamma_c$  outside the ring and no surfactant inside the ring initially. Again,  $t = 0$  s denotes the moment when the ring lifts. This experiment qualitatively resembles the one performed on a glycerol fluid layer. We also see the two Marangoni ridges in the footprint of the ring, as they move together to form a single central distension, which then relaxes away, over a much longer time than it took to form. It's important

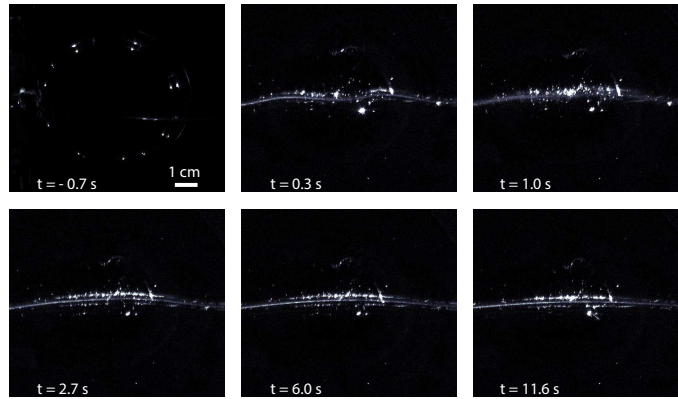


**Figure 4.2** Time series of images of an inward spreading data run on a glycerol fluid layer. Our initial concentration is  $\Gamma_0 = 0.8\Gamma_c$  outside the ring, and zero inside. The times of each frame are shown in the lower left hand corner of each, with  $t = 0$  being the moment when the ring is lifted. Note the progression of the Marangoni ridge visible in the laser line: soon after the ring has lifted, we see two ridges which soon join to a central distension, which then slowly relaxes. The many bright points in this image are reflective particles which are masked out in the image processing. Data recorded 02/07/14.

to note that the laser line is much thicker on a xanthan gum fluid layer than on glycerol. The xanthan gum particles suspended in the glycerol act as scatterers for the laser light. Because of this, the area of the image that is illuminated by the laser line is much greater than the spatial extent of the line itself. The laser is also much brighter in the images, which makes finding the height profile from the laser line easier.

## 4.2.2 Height and Intensity Profiles

### Height Profile

Our image processing code allows us to find the height profile as a function of time for a xanthan gum fluid layer. It works, essentially, because the xanthan gum mixture is opaque and scatters the light of the laser very effectively, so the laser appears very bright in our images. Experiments on a glycerol fluid layer, which is much more transparent, do not have such a visible laser line, and our laser line processing code hews to the brightest objects in the image, which tend to be dust particles illuminated by the laser. A clean experiment (i.e. one with no or very few particles in the fluid)

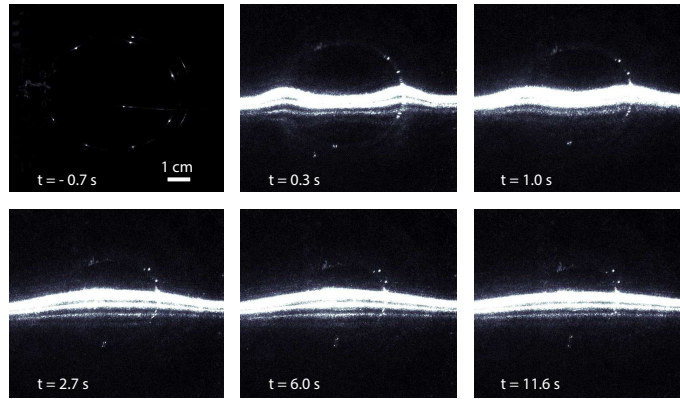
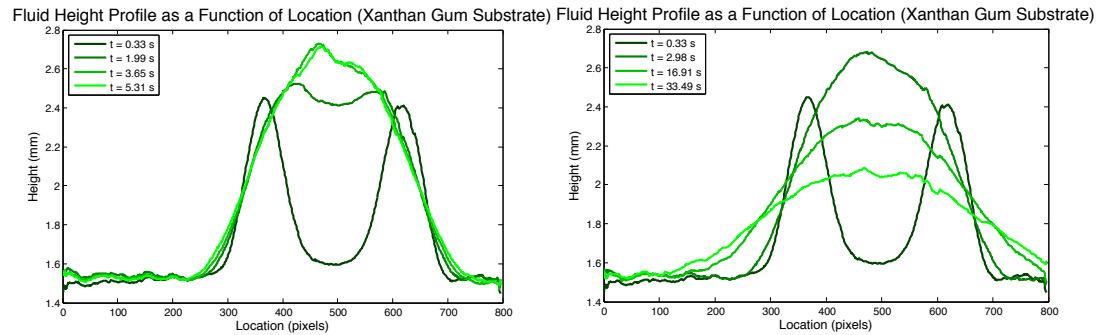


**Figure 4.3** Time series of images of a inward spreading data run on a 1.6 mm thick xanthan gum/glycerol mixture fluid layer. Our initial concentration is  $\Gamma_0 = 0.8\Gamma_c$  inside the ring, and zero outside. The times of each frame are shown in the lower left hand corner of each, with  $t = 0$  denoting the moment when the ring is lifted. Note the progression of the Marangoni ridge visible in the laser line: soon after the ring has lifted, we see two ridges which soon join to a central distension, which then slowly relaxes, just as in the case of the run on glycerol. Data recorded 02/20/14.

on glycerol may provide us with workable laser line data, but we have not been able to achieve such an experimental run as yet. It is, though, relatively simple to extract height profile data from an experiment on a xanthan gum fluid layer.

The fluid height profile extracted from an experiment on a xanthan gum fluid layer at various selected times can be seen in Fig. 4.4. The fluid layer begins in two similar distensions — the Marangoni ridges — which quickly move towards the middle and join into a central distension. The distension appears to form over a time frame of about three seconds, but doesn't fully decay over thirty more seconds. The dynamics of this height profile concur with our expectations and resemble those of Strickland et al. (2013). No obvious difference appears between our height profile from an experiment on xanthan gum and one collected on glycerol, and the general concurrence between our data and what we see happening in the images of the run inspires some confidence in our measured height profile.



- a. The initial Marangoni ridges occur at the location of the meniscus and move inward to form a central distension the height of which, after achieving its maximum, appears to remain constant over a short timescale.
- b. The central distension eventually does decay over long enough timescales, which are considerably longer than the time necessary for the central distension to form.

**Figure 4.4** Smoothed height profiles on a 1.6 mm xanthan gum fluid substrate as a function of spatial location in our image, plotted at four different times. Data was taken from an inward spreading run with initial concentration  $\Gamma_0 = 0.8\Gamma_c$  outside the ring and no surfactant inside. Data collected on 2/20/14.

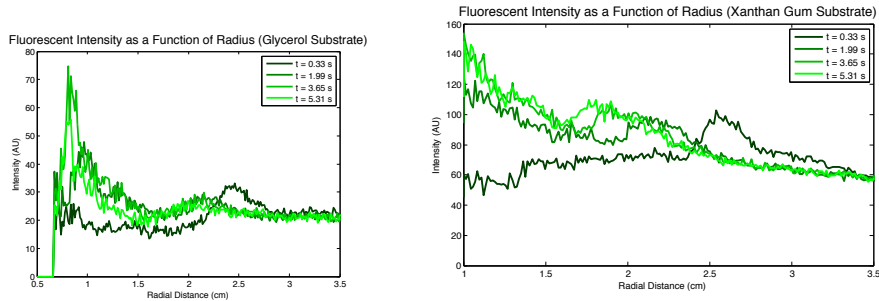
### Intensity Profile

The same cannot be said of intensity profiles we measured. We extracted intensity profiles — that is, the azimuthally averaged intensity of the image as a function of radial distance from the center of the experiment — from our images of both the xanthan gum and glycerol experiments. Each image in the series produces a profile for a single time; several such profiles can be seen in Fig. 4.5.

The plot shows the measured intensity versus radial distance in cm from the center at four times throughout a single run. This data was collected from inward spreading runs with  $\Gamma_0 = 0.8\Gamma_c$  outside the ring and  $\Gamma_0 = 0$  inside on a 1.6 mm thick layer of fluid layer (glycerol and xanthan gum for Fig. 4.5a and Fig. 4.5b, respectively).

In the ideal case, an intensity profile is due entirely to the fluorescence of the surfactant. Then, inversion from intensity to surfactant concentration, not even an easy task, becomes tractable. We may think that the intensity profiles we have extracted are representative of the fluorescent intensity in the system, but comparison with Fig. 4.6 suggests otherwise.

The maximum value of intensity measured for NBD-PC in our calibra-



- a. A plot showing measured intensity as a function of radius for four different short-term time values, taken from an experiment on a glycerol fluid layer. Note that the central peak on  $t$ . The bump here is the slight increase in intensity visible at  $r = 2.5$  cm at  $t = 0.33$  s that moves to the left and decreases in intensity as  $t$  increases, while the "peak" is the significant increase in intensity visible at  $r = 1$ . Data collected 02/11/14.
- b. A plot showing measured intensity as a function of radius for four different short-term time values, taken from an experiment on a xanthan gum fluid layer. The bump here is the slight increase in intensity visible at  $r = 2.5$  cm at  $t = 0.33$  s that moves to the left and increases in intensity as  $t$  increases, while the "peak" is the significant increase in intensity visible at  $r = 1$ . Data collected 02/20/14.

**Figure 4.5** A plot showing measured intensity as a function of radius for two different time values. Results are from inward spreading runs on a 1.6 mm thick layer of a glycerol (4.5a) or xanthan gum (4.5b) with initial surfactant concentration  $\Gamma_0 = 0.8\Gamma_c$  outside the ring, and no surfactant inside.

tion was an intensity of approximately 35 arbitrary units when the surfactant was at  $\Gamma_c$ . The maximum value of intensity in 4.5a is nearly twice that. Additionally, the average intensity of the profile to the left of the small bump at  $t = 0.33$  s appears to be around 20. If we take that to be all due to surfactant fluorescence, then it would imply that, less than one third of a second after the ring has lifted, almost all of the domain is near  $\Gamma = 0.7\Gamma_c$ . Considering that the initial condition is that  $\Gamma_0 = 0$  inside the ring, this seems highly unlikely. The images of the experimental run from which this profile is extracted in Fig. 4.2 reveal that, at  $t = 0.33$  s, the Marangoni ridge, which moves markedly faster than the surfactant, has not even yet covered the area inside the ring. This very strongly suggests that the intensity profile we calculate is not just due to the fluorescence of the surfactant.

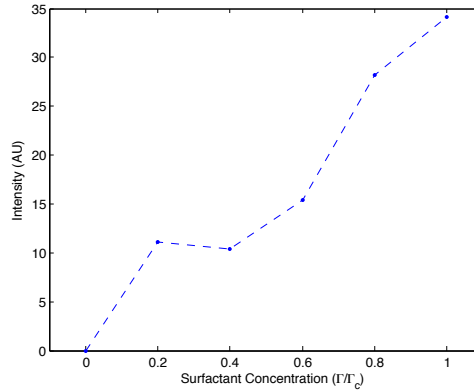


**Figure 4.6** Fluorescent intensity calibration for NBD-PC on a glycerol fluid layer. Note that the maximum intensity recorded, at  $\Gamma = \Gamma_c$ , is approximately half of the maximum intensity seen in 4.5a. Data taken 2/11/2014.

### Investigating the Peak in Intensity

If we rule out the fluorescence as the source of this intensity in the profile, and, given the magnitude of the intensity at the peak, it seems likely that this confounding intensity comes from the laser line. The peak intensity, though, is not constant. In fact, it rises fairly quickly and then decays in magnitude slowly. This suggests that there may be some connection between the central distension in the height profile, which follows the same type of growth and decay timescale. If there is a connection, then the Marangoni ridge is likely related to this confounding intensity. For the sake of exploring this relationship, we can plot the height profile of our xanthan gum experiment on concurrent axes with the intensity profile. This can be seen in Fig. 4.7.

There does appear to be some sort of correlation between the height of the fluid layer at  $r = 0$  and the height of the intensity peak. We can continue to explore this by plotting the distension height at  $r = 0$  against  $t$  concurrently with the maximum intensity over a small range near the minimum value of  $r$ , as can be seen in Fig.4.8.

This seems to show a correlation between the distension height and the magnitude of the peak at small  $r$ , at least up through approximately 30 seconds, although it does not clarify why these two quantities should be related. To attempt to resolve that, we should more closely examine the system. Fig.4.9 contains two images from this experiment at  $t = 4.31s$ , one

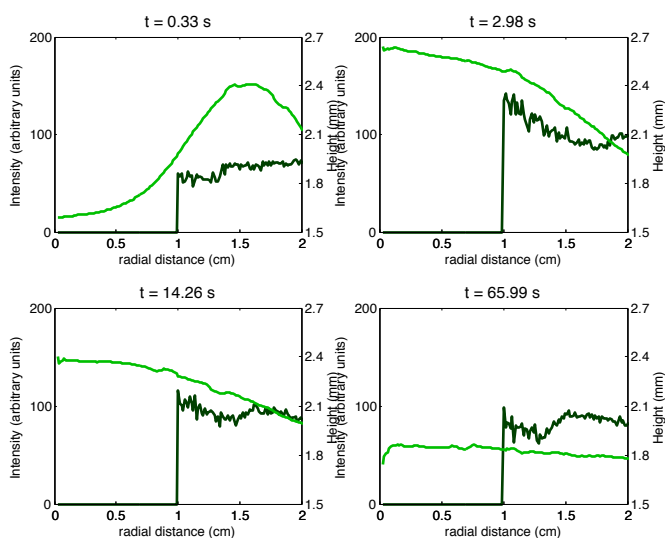


**Figure 4.7** Radial height and intensity profiles simultaneously plotted as functions of  $r$ , for four separate values of  $t$ . The smoothed height profile is plotted light green and the intensity profile is dark. Note the correspondence between the location of the height profile at  $r = 0$  and the height of the peak intensity near  $r = 1$ .

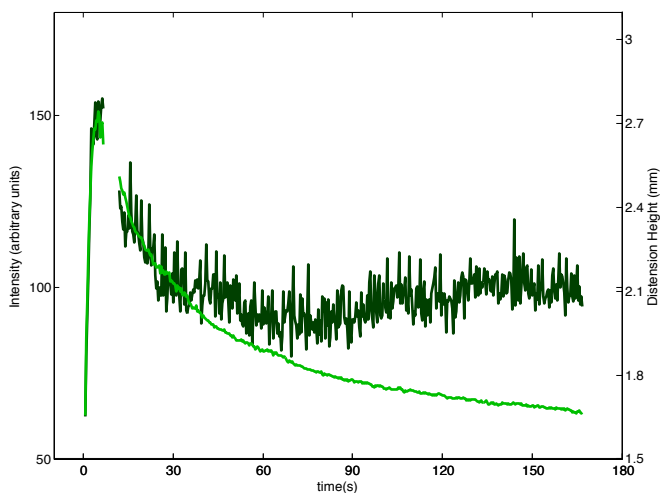


**Figure 4.8** Distension height at  $r = 0$  and peak Intensity near  $r = 1$  as functions of time. Both pieces of data are extracted from an inward spreading experiment on xanthan gum. NB: the lacuna in the data is due to a technical malfunction of the camera. Data taken 2/20/14.

masked as during the image analysis, and the other unmasked to show the laser line.

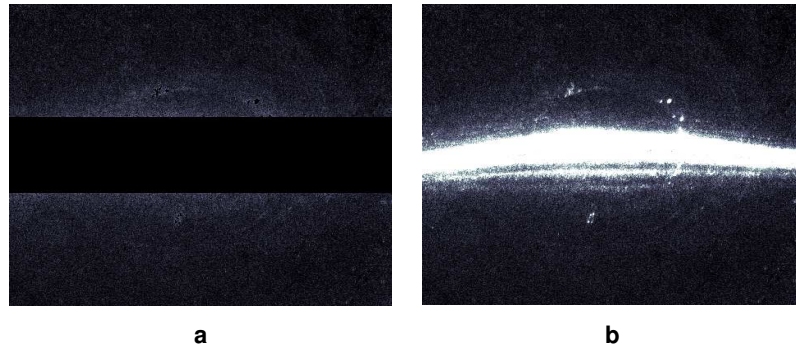


**Figure 4.9** Two images of an inward spreading experiment on a xanthan gum fluid layer with initial concentration  $\Gamma_0 = 0.8\Gamma_c$ . This is taken from an intermediate step of the image processing routine. The image on the left is masked required by the image processing. The image on the right is the same image with the mask removed. Note that the mask does block the spatial extent of the laser line, although it does not block all the light from the laser that is scattered by the xanthan gum.

The images that are processed to produce the intensity profile can clarify the source of the errant intensities. Recall that the xanthan gum suspension acts as an excellent scatterer of light, so the image of the laser line in the xanthan gum is much larger than just the spatial extent of the laser. Even though the mask in Fig. 4.9a covers the entire laser, some amount of scattered light is still visible around the edges of the mask.

This can explain the relationship the distension height and intensity peak at minimum  $r$ . The smallest value of  $r$  which is outside of the mask (and therefore included in the image processing) is equal to the length of the line that begins at the central point and terminates in a perpendicular intersection with the nearest mask edge. In the case of this image, that is a line directly up from the center to the top edge of the mask. The minimum  $r$  value points, then, are those points just outside the mask but aligned with the center.

When the distension height changes, it moves the image of the laser line in the plane of the image. As the central distension grows, it moves the laser line closer to the edge of the mask. While the spatial extent of the laser line might never exit the region that is masked out, the xanthan gum scatters enough light that a fair amount may exit the masked region. When

this light from the laser is scattered, it illuminates those points just outside the mask, causing the peak in intensity for small  $r$  that is prevalent in our data.

Although we have discovered the cause of the peak in our intensity profiles, we do not yet have a tangible explanation for the other aspect of the profile: the small bump.

### Surfactant Leading Edge

As we began our investigation of the intensity peak by considering timescales, we shall do the same for our investigation of the bump. We note that at early times in the profile it begins at the ring and moves inwards with apparently decreasing velocity as time evolves. This seems suggestive that the bump may in fact be due to surfactant fluorescence, as we would expect some evidence of that to be present in the profile.

Before we can argue that the bump in intensity is consistent with surfactant fluorescence behavior, we must have a good example of said behavior. Fig. 4.10 shows intensity profiles that were extracted from an inward spreading run conducted on 1.6 mm of xanthan gum with  $\Gamma_0 = 0.8\Gamma_c$  outside the ring and no surfactant inside, and no laser line. By eliminating the occlusive effects of the laser line on xanthan gum, we can calculate an intensity profile that is due only to the fluorescence.

We can see from Fig. 4.10 that, when the experiment is performed on a xanthan gum fluid layer without a laser line, the overall intensity is much lower—in fact, the intensity on xanthan gum seen therein is on the order of those seen in Fig. 4.5 for an experiment on glycerol. Discounting the small  $r$  peak due to the laser, the overall intensity is slightly higher on xanthan gum, which may be due to the scattering of LED light, but it is clear that most of the difference in the intensities between fluid layers comes from the image of the laser.

The data visible in Fig. 4.10 are actually what we expect our surfactant intensity data to look like, based on Strickland et al. (2013). It is interesting in that there is no clear qualitative difference between this data on xanthan gum and their data on glycerol. This implies that we can relate our data from the experiment without the laser to both of the other intensity profiles, at least in a general sense. This allows us to get a handle on the bump seen in both intensity profiles.

Note the similarity in position, relative height, and speed of the surfactant signal peak in Fig. 4.10 and the small bump in intensity in 4.5b. While this similarity is suggestive, we can get a better sense of their likeness if we

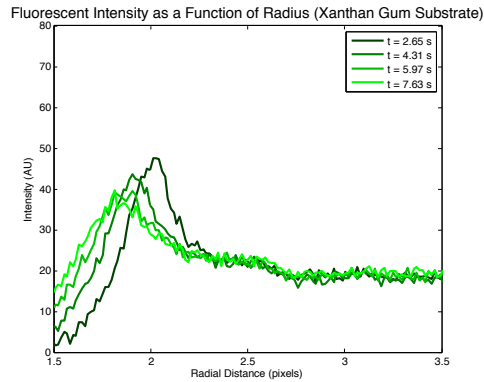


**Figure 4.10** Recorded intensity as a function of radial distance from the center of the ring, plotted at four different values of  $t$ . This data was extracted from an inward spreading run with on a 1.6 mm thick layer of a xanthan gum/glycerol mixture with initial surfactant concentration  $\Gamma_0 = 0.8\Gamma_c$  outside the ring, and no surfactant inside. Importantly, the laser line was off during the collection of this data, so the scattering of the laser by the xanthan gum mixture cannot be corrupting our data here. Note that the recorded intensity values here are much smaller than those in Fig. 4.5b. Data collected 4/10/14.

track their motion more quantitatively. We can track the surfactant leading edge of the dataset taken with no laser by finding the maximum value in a small range that includes the peak of the small bump visible in the figure, and then smooth the data. We track the tip of the small rise (assumed to be the approximate leading edge of surfactant) of the previous xanthan gum and glycerol data manually, by plotting the intensity data at a given time and using MATLAB's data cursor functionality to measure the position. This provides a rough estimate of the location of the leading edge; After approximately 8 seconds, the leading edge of the intensity in the glycerol experiment became too indistinct to attempt to measure its location. A plot of the resultant surfactant leading edge dynamics can be seen in Fig. 4.11.

Over a period from approximately 2.5 s to 13 s the two xanthan gum leading edges appear to coincide well, although they diverge after that before both more or less coming to rest at different radial distances from the center. This strongly suggests that the small bump we see in the intensity at short time scales in Fig. 4.5b is located approximately at the surfactant leading edge, and is in fact related to the surfactant fluorescence. We cannot come to the same conclusion for the experiment on glycerol, as the speed of

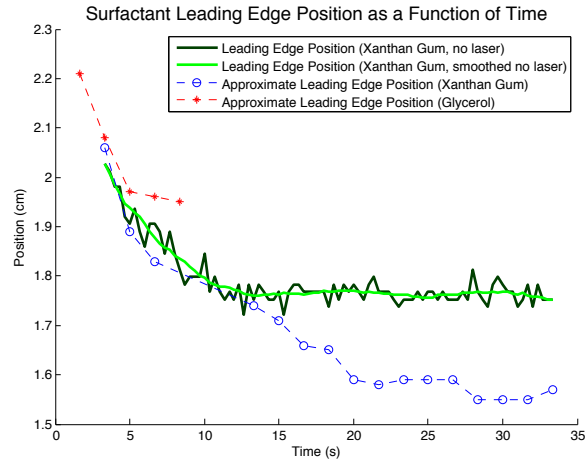


**Figure 4.11** Surfactant Leading Edge behavior for multiple datasets. The leading edge behavior calculated from the experiment on xanthan gum without a laser line is in green, while those manually measured from experiments on glycerol and xanthan gum are in red and blue, respectively. The lacuna in the blue xanthan gum data is again due to a camera malfunction.

the leading edge appears to slow much earlier than the comparable velocity on xanthan gum, and furthermore the number of data points is inadequate to say anything about longer term behavior. It does, though, seem unlikely that we would have such apparently similar behavior visible if the cause were completely unrelated.



# Chapter 5

## Conclusion

### 5.1 Discussion of Results

When I entered the lab at the beginning of this year, we had the technical ability to perform experimental runs and take data, although we had as of that point not produced any quantitative data. Over the course of this research, we not only collected valuable quantitative data, but we also improved the apparatus to make it easier to do so in the future. We also advanced the experiment by improving the apparatus and changing the fluid layer to one that is shear thinning and collecting both intensity profile and height profile data for that fluid layer.

We made an attempt to simultaneously measure the height profile and intensity profile on both glycerol and xanthan gum fluid layers, although this was not as successful. Instead of seeing the relatively simple intensity profile visible on the no-laser experiment, we saw a set of intensity profiles with two prominent peaks: one smaller, whose location appeared to coincide with the surfactant fluorescent intensity peak visible in the no-laser experiment; and one larger intensity peak, which occurred at values of small  $r$ . Numerical comparison of the location of the smaller peak from the experiment on xanthan gum to the peak visible in the no-laser intensity profile suggests that the smaller intensity peak is caused by the surfactant and is roughly coincident with the leading edge of surfactant. While we don't have a comparison to make to the experiment performed on glycerol, we also have no reason to believe that such a similar structure would appear in the intensity profile for that experiment and not be related to the leading edge of surfactant. As we have not yet seen a qualitative difference between experiments on glycerol and xanthan gum, we cannot reasonably

conclude that these profiles are qualitatively different. We can at least measure some intensity signal from the surfactant fluorescence, although the central intensity peak presents issues.

The larger, more central intensity peak was due to the formation of the central distension causing the image of the laser, or a nearby object or region highly illuminated by it, to move out of the region we mask for the laser line. This is revealed especially by simultaneously observing the height of the distension at  $r = 0$  and the magnitude of the central intensity peak as functions of time; this observation reveals them to, over a period of about 30 s and when scaled appropriately, align nearly perfectly, implying that the height of the central distension is directly related to the intensity of the central peak. It is not the laser line that directly causes this peak in measured intensity, rather it is light scattered from the laser line. On a glycerol fluid layer, the only significant scatterers are particles in the fluid, but the xanthan gum mixture we use is a relatively opaque suspension of xanthan gum particles in glycerol, so the fluid is itself a scatterer. Because the presence of the laser line affects the intensity profile so drastically, our simultaneous measurement regime can be problematic. For glycerol, the laser only creates an issue with the intensity profile if there are scatterers, e.g. dust particles, in the fluid. Thus, a very clean experiment performed on glycerol should be sufficient to overcome this issue. On a xanthan gum fluid layer, though, the issue is harder to address, in that we cannot make the fluid layer any less opaque. Because we know the distension is very closely related to this central intensity peak for the first 30 s, it may be possible to use information gained from the height profile to calculate the central intensity peak and then somehow remove it from the intensity profile to recover only the surfactant behavior. This is worth investigating, as the simultaneous measurement of the fluid height and intensity profiles is a considerable strength of our experiment.

## 5.2 Future Work

The simultaneous collection of height and intensity profiles on xanthan gum will likely prove more difficult than simply having a clean experimental run. It may be possible to use the height profile data, which is relatively easy to extract, in order to collect and clean the intensity profile data and resolve the issue of simultaneous measurement on a xanthan gum fluid layer. We should first investigate if this approach is even possible. If such a technique is successful, the data we already have may be sufficient for a

proof of concept, but we would need to perform more experimental runs on xanthan gum fluid layers to ensure that the any method we devise is robust.

The height profile data we do have raises interesting questions about the effect of the meniscus. In order to examine the effect of the meniscus, an experiment in which the same concentration of surfactant is placed outside as well as inside the ring should be performed under the hypothesis that the uniform surfactant concentration field should give rise to no Marangoni effects. Doing so, we can isolate the effect of the meniscus on the concentration of surfactant and fluid height profile. This experiment should be performed on both fluid layers to determine if the effect of the meniscus depends on the fluid.

It is somewhat premature to refer to the collection of surfactant concentration data, as we have not yet successfully inverted the fluorescent intensity to surfactant concentration relationship. This is an important future step for our research group. There are several possible approaches. One is based in the image processing code, and the other is a more physical approach. It may be possible to perform an accurate inversion despite the non-monotonicity of the intensity/concentration relationship if one assumes continuity of surfactant concentration in space and time and a known concentration somewhere in the profile. This computational inversion procedure would be an important step forward, and should be investigated.

The more physical approach worth considering is using a mixture of surfactants rather than pure NBD-PC. The non-monotonicity is a result of quenching effects due to FRET, which occurs when fluorescent molecules are too highly concentrated. If we mix NBD-PC with a non-fluorescent surfactant such as POPC or DHPE, we may be able to maintain surfactant concentration while reducing the concentration of fluorescent molecules, and avoid quenching and FRET effects among the NBD-PC molecules. This will raise many technical questions including whether such a mixture will have the same surfactant properties as pure NBD-PC, and whether FRET effects can really be eliminated. This will require experiments to be run on a Langmuir-Blodgett trough, as well as many surfactant fluorescence calibration images.

One large question that remains unanswered is about the fluid properties of our xanthan gum mixture. While Ciullo and Flynn (2000) states that our mixture, as we have prepared it, is shear-thinning, it is important that we verify their findings. Attempting to do so will require access to a shear rheometer, which we currently do not have. Having access to a shear

rheometer will allow us to more precisely know the exact nature of our fluid layer, which will be important when it comes time to compare those to an eventual model.

Finally, there remains the ongoing task of improving the apparatus further. One glaringly necessary improvement involves removing the LEDs from the well and mounting them permanently on the apparatus, as the constant handling of the LED circuit has caused some failures in the circuit that have cost us significant amounts of lab time. Installing the LED circuit more permanently would make it more robust, and thus save us the lab time require to fix the circuit when it breaks. In addition, a more permanent solution to the problem of dust falling into the well should be looked into. These improvements to the apparatus will help us collect more, and more consistent, data on this system.

# Bibliography

2013. Avanti polar lipids catalogue. Website. URL [http://www.avantilipids.com/index.php?option=com\\_content&view=article&id=1027&Itemid=220&catnumber=810130](http://www.avantilipids.com/index.php?option=com_content&view=article&id=1027&Itemid=220&catnumber=810130).

Bull, JL, LK Nelson, JT Walsh Jr, MR Glucksberg, S Schürch, JB Grotberg, et al. 1999. Surfactant-spreading and surface-compression disturbance on a thin viscous film. *Journal of biomechanical engineering* 121(1):89–98.

Çengel, Yunus A., and John M. Cimbala. 2013. *Fluid Mechanics: Fundamentals and Applications*. McGraw-Hill.

Ciullo, Peter A., and Frank Flynn. 2000. Thickening glycerol, naturally. *Personal Care* .

Fallest, David W, Adele M Lichtenberger, Christopher J Fox, and Karen E Daniels. 2010. Fluorescent visualization of a spreading surfactant. *New Journal of Physics* 12(7):073,029.

Gaver, Donald P, and James B Grotberg. 1990. The dynamics of a localized surfactant on a thin film. *J Fluid Mech* 213(1):127–148.

Hargreaves, T. 2003. Surfactants: the ubiquitous amphiphiles. *Chemistry World* .

Kumar, Shreyas Depuma. 2014. *Simulations of Surfactant Driven Thin Film Flow*. Senior thesis, Harvey Mudd College.

Pockels, Agnes, and Lord Rayleigh. 1891. Surface tension. *Nature* 43:437–439.

Salager, J-L. 2002. Surfactants: Types and uses. Universidad De Los Andes.

- Segur, John Bartlett, and Helen E Oberstar. 1951. Viscosity of glycerol and its aqueous solutions. *Industrial & Engineering Chemistry* 43(9):2117–2120.
- Selvin, Paul R. 2000. The renaissance of fluorescence resonance energy transfer. *Nature Structural Biology* 7(9):730. URL <http://search.ebscohost.com/login.aspx?direct=true&db=aph&AN=8817306&site=ehost-live&scope=site>.
- Shrive, Jason DA, John D Brennan, R Stephen Brown, and Ulrich J Krull. 1995. Optimization of the self-quenching response of nitrobenzoxadiazole dipalmitoylphosphatidylethanolamine in phospholipid membranes for biosensor development. *Applied spectroscopy* 49(3):304–313.
- Song, Ki-Won, Yong-Seok Kim, and Gap-Shik Chang. 2006. Rheology of concentrated xanthan gum solutions: Steady shear flow behavior. *Fibers and Polymers* 7(2):129–138. doi:10.1007/BF02908257. URL <http://dx.doi.org/10.1007/BF02908257>.
- Stevens, Timothy P, and Robert A Sinkin. 2007. Surfactant replacement therapy. *CHEST Journal* 131(5):1577–1582.
- Strickland, Stephen L, Matthew Hin, M Richard Sayanagi, Cameron Conti, Karen E Daniels, and Rachel Levy. 2013. Self-healing dynamics of surfactant coatings on thin viscous films. Preprint.
- Swanson, Ellen. 2010. *Flow of Thin Liquid Films with Surfactant: Analysis, Numerics, and Experiment*. Phd thesis, North Carolina State University.
- Troian, S. M., X. L. Wu, and S. A. Safran. 1989. Fingering instability in thin wetting films. *Phys Rev Lett* 62:1496–1499. doi:10.1103/PhysRevLett.62.1496. URL <http://link.aps.org/doi/10.1103/PhysRevLett.62.1496>.
- Zhong, L., M. Oostrom, M.J. Truex, V.R. Vermeul, and J.E. Szecsody. 2013. Rheological behavior of xanthan gum solution related to shear thinning fluid delivery for subsurface remediation. *Journal of Hazardous Materials* 244–245(0):160–170. doi:<http://dx.doi.org/10.1016/j.jhazmat.2012.11.028>. URL <http://www.sciencedirect.com/science/article/pii/S0304389412011193>.